ALZHEIMER'S DISEASE

An epoxide hydrolase inhibitor reduces neuroinflammation in a mouse model of Alzheimer's disease

Anamitra Ghosh[1], Michele M. Comerota[1], Debin Wan[2], Fading Chen[1], Nicholas E. Propson[1,3], Sung Hee Hwang[2], Bruce D. Hammock[2], Hui Zheng[1,3,4]*

Neuroinflammation has been increasingly recognized to play a critical role in Alzheimer's disease (AD). The epoxy fatty acids (EpFAs) are derivatives of the arachidonic acid metabolism pathway and have anti-inflammatory activities. However, their efficacy is limited because of their rapid hydrolysis by the soluble epoxide hydrolase (sEH). We report that sEH is predominantly expressed in astrocytes and is elevated in postmortem brain tissue from patients with AD and in the 5xFAD β amyloid mouse model of AD. The amount of sEH expressed in AD mouse brains correlated with a reduction in brain EpFA concentrations. Using a specific small-molecule sEH inhibitor, 1-trifluoromethoxyphenyl-3-(1-propionylpiperidin-4-yl) urea (TPPU), we report that TPPU treatment protected wild-type mice against LPS-induced inflammation in vivo. Long-term administration of TPPU to the 5xFAD mouse model via drinking water reversed microglia and astrocyte reactivity and immune pathway dysregulation. This was associated with reduced β amyloid pathology and improved synaptic integrity and cognitive function on two behavioral tests. TPPU treatment correlated with an increase in EpFA concentrations in the brains of 5xFAD mice, demonstrating brain penetration and target engagement of this small molecule. These findings support further investigation of TPPU as a potential therapeutic agent for the treatment of AD.

INTRODUCTION

Alzheimer's disease (AD) is the most common form of age-associated neurodegenerative disorder pathologically defined by the deposition of extracellular beta amyloid (Aβ) plaques and the accumulation of intracellular neurofibrillary tangles (*1*). Overwhelming evidence supports a crucial role of Aβ in initiating a cascade of pathogenic events leading to cognitive impairment and neurodegeneration (*2*, *3*). Hence, the majority of AD clinical trials have been focused on Aβ. Unfortunately, these trials have been unsuccessful so far (*2*, *4*–*6*). Thus, there is an urgent need to pursue other disease-modifying therapies.

Besides the pathological hallmarks, AD is associated with prominent neuroinflammation (*7*, *8*). Prolonged activation of glial cells, microglia, and astrocytes, in particular, and the release of proinflammatory cytokines, chemokines, and reactive oxygen and nitrogen species create a neurotoxic environment, which could exacerbate the progression of AD (*9*–*11*). Recent genome-wide association studies identified multiple immune-related gene variants as risk factors for late-onset AD, supporting a major contributing role of innate immunity and neuroinflammation in AD (*12*–*15*). However, although epidemiological studies indicated positive effects of nonsteroidal anti-inflammatory drugs such as cyclooxygenase (COX) inhibitors in AD protection, randomized clinical trials failed to demonstrate clinical efficacy (*16*, *17*).

COX, along with lipoxygenase (LOX) and cytochrome P450 monooxygenase (CYP), belongs to the arachidonic acid metabolic pathway that produces prostaglandins, leukotrienes, and various epoxy fatty acids (EpFAs) including epoxyeicosatrienoic acids (EETs) and epoxydocosapentaenoic acids (EDPs) from arachidonic acid (*18*, *19*). Among these, the COX and LOX pathways have been extensively studied and successfully targeted therapeutically (*18*). In contrast, much less is known about the therapeutic potential of targeting the CYP pathway.

EETs and EDPs have been demonstrated to have anti-inflammatory and neuroprotective properties through multiple mechanisms. EETs inhibit vascular cell adhesion molecule–1, E-selectin, and intercellular adhesion molecule–1 expression in endothelial cells to block monocyte infiltration (*20*). By inhibiting nuclear factor κB (NF-κB) nuclear translocation, EpFAs down-regulate several proinflammatory molecules including the inducible nitric oxide (iNOS) and COX-2 (*20*–*22*). Further, EETS and EDPs have been shown to reduce inflammation and neurodegeneration by acting on signal transducer and activator of transcription 3 and nuclear hormone receptors such as peroxisome proliferator–activated receptor alpha and gamma (*23*, *24*). However, EpFAs are broken down rapidly into corresponding diols by the soluble epoxide hydrolase (sEH). sEH, encoded by the *EPHX2* gene, contains an N-terminal phosphatase and a C-terminal hydrolase domain and exists as a homodimer (*25*). sEH is widely expressed in both peripheral tissues and central nervous system (CNS). Elevated sEH expression has been reported in CNS disorders such as depression (*26*), schizophrenia (*27*), Parkinson's disease (*28*), and recently AD (*29*, *30*). sEH inhibition by genetic deletion or pharmacological blockade has been shown to confer beneficial effects in mouse models of these diseases, but few mechanistic insights have been provided. Whether these effects are associated with changes in EpFAs remains unclear.

Here, we present evidence that sEH is aberrantly elevated in postmortem brain tissue from patients with AD and in β-amyloid precursor protein (APP)/Aβ transgenic and knock-in mouse models of AD. Using a selective sEH inhibitor, 1-trifluoromethoxyphenyl-3-(1-propionylpiperidin-4-yl) urea (TPPU), that specifically inhibits the C-terminal hydrolase activity of the sEH (*26*, *31*), we demonstrate

[1]Huffington Center on Aging, Baylor College of Medicine, Houston, TX 77030, USA. [2]Department of Entomology and Nematology and UCDMC Comprehensive Cancer Center, University of California, Davis, CA 95616, USA. [3]Department of Molecular and Cellular Biology, Baylor College of Medicine, Houston, TX 77030, USA. [4]Department of Molecular and Human Genetics, Baylor College of Medicine, Houston, TX 77030, USA. *Corresponding author. Email: huiz@bcm.edu

that long-term administration of TPPU to the 5xFAD mouse model of AD restored EpFA concentrations and reversed microglia and astrocyte reactivity in mouse brain. These changes were accompanied by attenuated Aβ pathology and improved synaptic integrity and cognitive function in the AD mouse model.

RESULTS

Elevated sEH and diminished EpFA in postmortem mouse and human brains

Arachidonic acid is an omega-6 unsaturated fatty acid released from the membrane phospholipids by phospholipase A2 (PLA_2) or derived from endocannabinoids by fatty acid amide hydrolase (FAAH) and can be further metabolized by COX, LOX, or CYP (fig. S1A) (*32*). We first evaluated the expression of arachidonic acid metabolic pathway genes in postmortem AD brain samples and those of age-matched controls without dementia. Quantitative real-time polymerase chain reaction (qPCR) analysis showed that the expression of *PLA2G2A*, but not *FAAH*, was elevated in postmortem AD human brains (fig. S1B), suggesting that PLA_2-mediated release, but not endocannabinoid conversion, may be a driver for changes in arachidonic acid metabolism in AD. Expression of both the *COX2* and *CYP4F8* genes, which produce prostaglandin and its metabolite prostaglandin E_2, respectively, was increased, suggesting overall activation of the COX pathway. Examination of the CYP monooxygenase pathway revealed that, whereas no differences in several of the CYPs, including *CYP2J2*, *CYP2C8*, and *CYP2C19*, were detected, expression of *EPHX2* was higher in AD postmortem brain samples compared to control brain samples (fig. S1B).

Consistent with the mRNA expression, Western blot analysis revealed a nearly twofold increase of sEH protein in postmortem AD brains compared to control brains (Fig. 1, A and B). Elevated *Ephx2* mRNA (Fig. 1C) and sEH protein (Fig. 1, D and E) were also detected in the cortex and hippocampus of 5xFAD transgenic mice at 4.5 months of age compared to their littermate nontransgenic controls. This result was further validated in an APP^{NLGF} knock-in mouse model of AD with physiological expression of APP (fig. S1, C and D) (*33*). Consistent with elevated sEH, lipodomics analysis of two major sEH EpFA substrates, EETs and EDPs, by liquid chromatography–tandem mass spectrometry (LC-MS/MS) showed a reduction in multiple EET and EDP regioisomers in transgenic mouse brains in comparison to nontransgenic control mouse brains (Fig. 1F). Thus, heightened sEH expression was a common feature in human AD and APP/Aβ mouse brain samples, which in 5xFAD mice resulted in reduced EpFAs.

TPPU and EETs block astroglial sEH up-regulation and lipopolysaccharide-induced inflammation in vitro

To assess the cell-type expression of sEH, we used a flow cytometry–based concurrent brain cell-type acquisition (CoBrA) method to simultaneously isolate astrocytes, microglia, and vascular endothelial cells from 4.5-month-old nontransgenic control and 5xFAD transgenic mouse brains (*34*). qPCR analysis revealed that *Ephx2* was highly expressed in sorted astrocytes and that expression was higher in transgenic compared to nontransgenic mice (Fig. 2A). In contrast, *Ephx2* expression was lower in microglia and endothelial cells, and no substantial changes were detected between transgenic and nontransgenic mouse brain samples (Fig. 2A). This result was substantiated by coimmunofluorescence staining for sEH and astrocyte [glial fibrillary acidic protein (GFAP)] or microglia (Iba-1) markers in hippocampal sections of nontransgenic control and 5xFAD transgenic mouse brains (Fig. 2B). We observed elevated expression of sEH predominantly in GFAP-positive astrocytes in transgenic mouse brain samples, with negligible costaining with Iba-1. Both the sEH fluorescence intensity and the number of sEH-expressing cells were increased in 5xFAD transgenic compared to nontransgenic control mouse brains (Fig. 2C). Similar astrocytic up-regulation of sEH was also observed after acute lipopolysaccharide (LPS) administration in vivo (fig. S2) and in primary astrocyte cultures (fig. S3, A and B). Next, we tested the effect of the sEH inhibitor TPPU in LPS-treated mouse primary astrocyte cultures. Thirty minutes of TPPU treatment dose-dependently reduced nitrite release as measured by the Griess assay (Fig. 2D) and reduced the expression of proinflammatory molecules *Il-1α*, *Il-1β*, *Tnf-α*, *Il-6*, *iNOS* and *Gfap* (Fig. 2E), and *Ccl-2* and *Cxcl-1* (fig. S3C). The reduced expression of iNOS and GFAP was confirmed by immunostaining (Fig. 2, F and G).

Next, we wondered whether the anti-inflammatory effect of sEH inhibition could be attributed to increased EETs. Although a membrane receptor for EET has yet to be identified, epoxyeicosa-5(Z)-enoic acid (EEZE) has been reported to act as a direct EET antagonist on the cell membrane or intracellularly (*35*) where it blocks the vascular actions of the EETs (*36*, *37*) and the anti-inflammatory effects of the sEH inhibitor 12-(3-adamantane-1-yl-ureido)-dodecanoic acid in cultured microglia (*38*). We thus tested the effect of EEZE by pretreating the mouse primary astrocytes with TPPU or 14,15-EEZE for 30 min before LPS treatment and measuring nitrite release by the Griess assay. The inhibitory effect of TPPU was completely abolished upon cotreatment with 14,15-EEZE (Fig. 2H), suggesting that EETs may be the functional mediators of TPPU's effects. Supporting this assessment, a 30-min pretreatment of mouse primary astrocyte cultures with 11,12-EET attenuated LPS-induced nitrite release in a dose-dependent manner (Fig. 2I).

In agreement with the astroglial-specific expression of sEH, TPPU had no effect on LPS-treated mouse primary microglia cultures measured by the expression of proinflammatory molecules (Fig. 3A) or iNOS induction (Fig. 3, B and C). However, when the same TPPU treatment was applied to mixed mouse astrocyte and microglia cultures, TPPU attenuated iNOS production in both cell types (Fig. 3, D and E) and reduced cytokine expression (Fig. 3F), suggesting that TPPU may act on astrocytes to suppress microglial reactivity through secreted EETs. Direct EET treatment of mouse primary microglia monocultures also blocked LPS-induced reactive nitrogen species (Fig. 3G) and the expression of the proinflammatory molecules *Il-1α*, *Il-1β*, *Tnf-α*, *Il-6*, *iNOS*, and *C3* (fig. S4). The efficacy of EET in preventing LPS-induced cytokine expression was further validated using an ex vivo mouse hippocampal organotypic slice culture system (fig. S5). Collectively, these results suggest a mechanism whereby TPPU inhibited astroglial sEH activity, and the resulting augmentation of EETs exerted anti-inflammatory effects in both astrocytes and microglia through autocrine and paracrine activities.

TPPU mitigates LPS-induced acute inflammation in vivo

Given the anti-inflammatory effects of TPPU in vitro, we next assessed its in vivo efficacy. We first examined whether TPPU is a substrate for P-glycoprotein, which mediates the adenosine triphosphate–dependent efflux of drugs or xenobiotics (*39*). Using the well-established human Caco-2 cell line (*40*, *41*), we determined

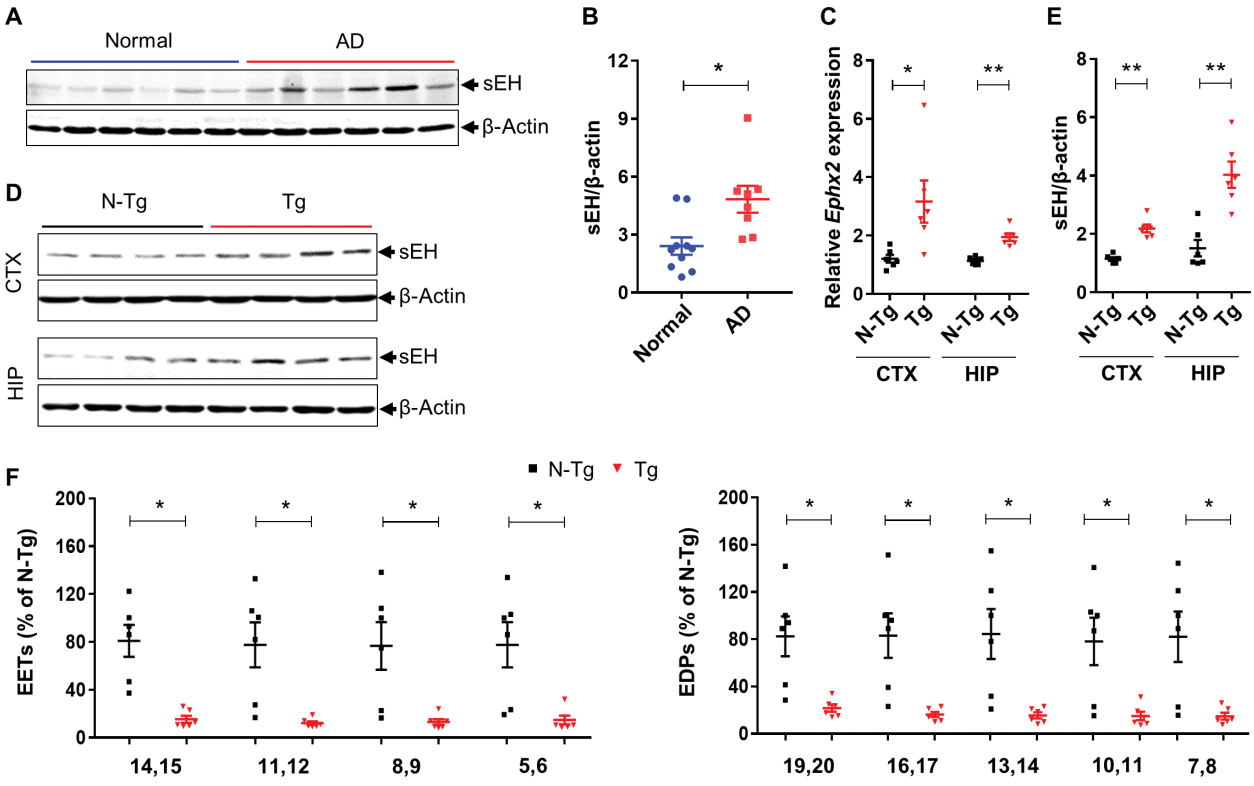

Fig. 1. Dysregulation of sEH and EETs in AD. (**A**) Representative Western blot illustrating the expression of sEH in postmortem brain tissue from patients with AD ($n = 6$) and age-matched cognitively normal controls ($n = 6$). β-Actin was used as a loading control. (**B**) Quantification of the sEH/β-actin ratio in the Western blot from (A). (**C**) qPCR analysis of *Ephx2* expression in cortex (CTX) and in hippocampus (HIP) of littermate nontransgenic (N-Tg) and 5xFAD transgenic (Tg) mice at 4.5 months of age. (**D**) Representative Western blot illustrating the amount of Ephx2 in cortex and hippocampus of 5xFAD transgenic and nontransgenic control mice. β-Actin was used as a loading control. (**E**) Quantification of sEH/β-actin ratio in mouse cortex and hippocampus in the Western blot in (D). (**F**) Quantification of relevant EET and EDP regioisomers (as a percentage of concentrations in nontransgenic mouse brain) in 5xFAD transgenic and nontransgenic control mouse brains. The numbers on the *x* axis denote carbon numbers where the double bonds were located in the corresponding polyunsaturated fatty acids. Data are means ± SEM of 8 to 10 human postmortem brain tissue samples per group (A and B and table S2) or 6 to 8 mice per group of mixed gender (C to F). $^{**}P < 0.01$ and $^{*}P < 0.05$. Data were analyzed by unpaired Student's *t* test.

that the apparent permeability coefficient (P_{app}) for TPPU from the basolateral to the apical surface of Caco-2 cells in culture was 24.45 × 10^{-6} cm/s and from the apical to the basolateral surface was 18.03 × 10^{-6} cm/s (table S1). Thus, the overall efflux ratio was 1.36, which was decreased to 0.99 in the presence of verapamil, a P-glycoprotein inhibitor. Given that a ratio of >2 is generally considered to involve P-glycoprotein–mediated efflux (*41*), TPPU is unlikely to be a favorable P-glycoprotein substrate.

Next, we investigated the effect of TPPU on LPS-induced inflammation by first treating C57BL/6 wild-type mice with TPPU (3 mg/kg) via oral gavage for 24 hours, which was then followed by cotreatment with LPS [3 mg/kg, intraperitoneally (i.p.)] and TPPU (3 mg/kg, oral gavage) for 18 hours (fig. S6A). Consistent with the in vitro and ex vivo studies, qPCR analysis of mouse brain samples showed that LPS triggered the expression of proinflammatory molecules in both the cortex and the hippocampus, the majority of which were reduced by TPPU (fig. S6B). Western blotting showed that expression of iNOS, COX-2, GFAP, Iba-1, and sEH were up-regulated in LPS-treated mice but down-regulated by TPPU in both the hippocampus and the cortex (fig. S6, C to F). Immunofluorescence staining of Iba-1 and GFAP and costaining with COX-2 and iNOS documented that TPPU treatment mitigated LPS-induced microglia and astrocyte staining intensities as well as COX-2 and iNOS immunoreactivities (fig. S7). The anti-inflammatory effect of sEH antagonism was further validated using another sEH inhibitor, EC5026 (fig. S8). Together, the results suggest that sEH blockade by TPPU may prevent acute neuroinflammation in vitro and in vivo.

TPPU enters the brain and engages its target under chronic treatment conditions in mice

Given the heightened expression of sEH in AD postmortem human brains and AD mouse models and the acute anti-inflammatory effect of TPPU, we next tested the long-term effect of TPPU treatment in the 5xFAD transgenic mouse model. We chose to start the treatment at 2 months of age because increased *Ephx2* expression was detected at this age and remained relatively stable for up to 15 months (fig. S9). We supplied either vehicle or TPPU to 5xFAD transgenic mice and their nontransgenic littermate controls via drinking water continuously for 2.5 or 4.5 months (fig. S10A). Measurement of average water consumption per week per mouse for 10 weeks found no substantial differences between the vehicle-treated and TPPU-treated transgenic mouse groups, demonstrating that TPPU did not affect fluid intake (fig. S10B). Measurement of TPPU in brain and plasma samples showed that, whereas TPPU was undetectable in vehicle-treated control brain and plasma samples, its concentration could be measured in the brain (fig. S10C) and plasma of TPPU-treated mice (fig. S10D). The resulting brain-to-plasma ratio was 21.7 and 17.2% for the nontransgenic and transgenic mouse

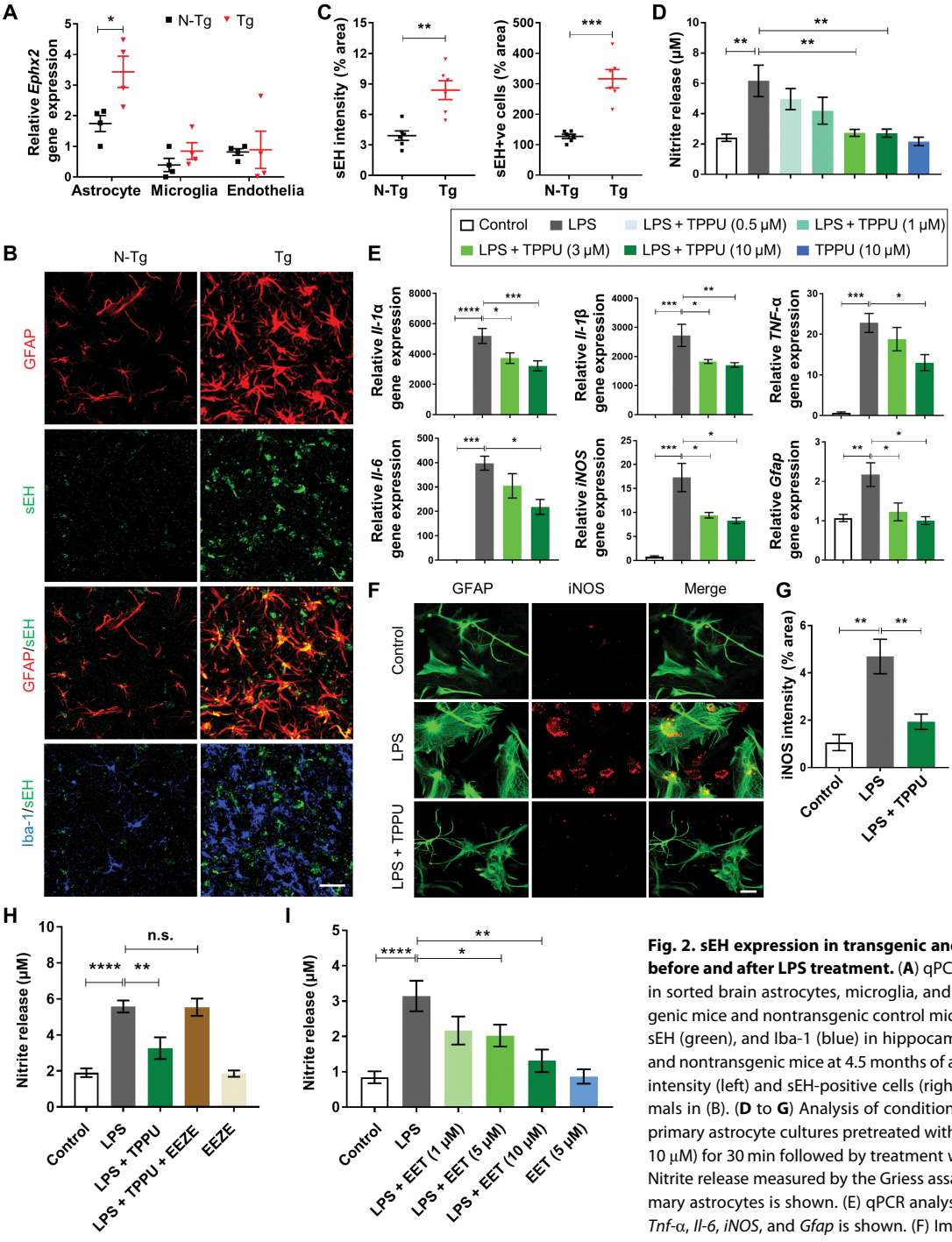

Fig. 2. sEH expression in transgenic and nontransgenic mouse astrocytes before and after LPS treatment. (**A**) qPCR analysis of *Ephx2* mRNA expression in sorted brain astrocytes, microglia, and vascular endothelia of 5xFAD transgenic mice and nontransgenic control mice. (**B**) Immunostaining of GFAP (red), sEH (green), and Iba-1 (blue) in hippocampal sections from 5xFAD transgenic and nontransgenic mice at 4.5 months of age. (**C**) Quantification of sEH staining intensity (left) and sEH-positive cells (right) in hippocampal sections from animals in (B). (**D** to **G**) Analysis of conditioned medium or cell lysates of mouse primary astrocyte cultures pretreated with different doses of TPPU (from 0.5 to 10 μM) for 30 min followed by treatment with LPS (100 ng/ml) for 24 hours. (D) Nitrite release measured by the Griess assay in media from cultured mouse primary astrocytes is shown. (E) qPCR analysis of mRNA expression of *Il-1α*, *Il-1β*, *Tnf-α*, *Il-6*, *iNOS*, and *Gfap* is shown. (F) Immunocytochemistry of GFAP (green) and iNOS (red) expression in cultured mouse primary astrocytes and (G) quantification of iNOS intensity are shown. (**H**) Nitrite release was measured by the Griess assay in conditioned media from cultured mouse primary astrocytes pretreated with TPPU (10 μM) or the pan-EET receptor antagonist 14,15-EEZE (1 μM) for 30 min followed by LPS treatment (100 ng/ml) for 24 hours. (**I**) Nitrite concentrations in conditioned media from cultured mouse primary astrocytes pretreated with different doses of 11,12-EET (from 1 to 10 μM) for 30 min followed by LPS treatment (100 ng/ml) for 24 hours are shown. Data are means ± SEM of four to six mice per group of mixed gender (A to C) or three independent experiments (D to I). ****$P < 0.0001$, ***$P < 0.001$, **$P < 0.01$, and *$P < 0.05$; n.s., not significant. Data were analyzed either by unpaired Student's *t* test (A and C) or by one-way ANOVA with Tukey's multiple comparison test (D, E, and G to I). Scale bar, 50 μm (B) and 100 μm (F).

groups, respectively, similar to the ratio reported after acute administration (*26*). These results established that TPPU was able to gain access to the mouse brain where its concentration could be maintained under chronic treatment conditions.

To determine the target engagement of TPPU in the mouse brain, we measured the concentration of EETs and EDPs, which were reduced in 5xFAD transgenic mouse brains (Fig. 1F). We found that the EETs (Fig. 4A) and EDPs (Fig. 4B) were elevated in TPPU-treated

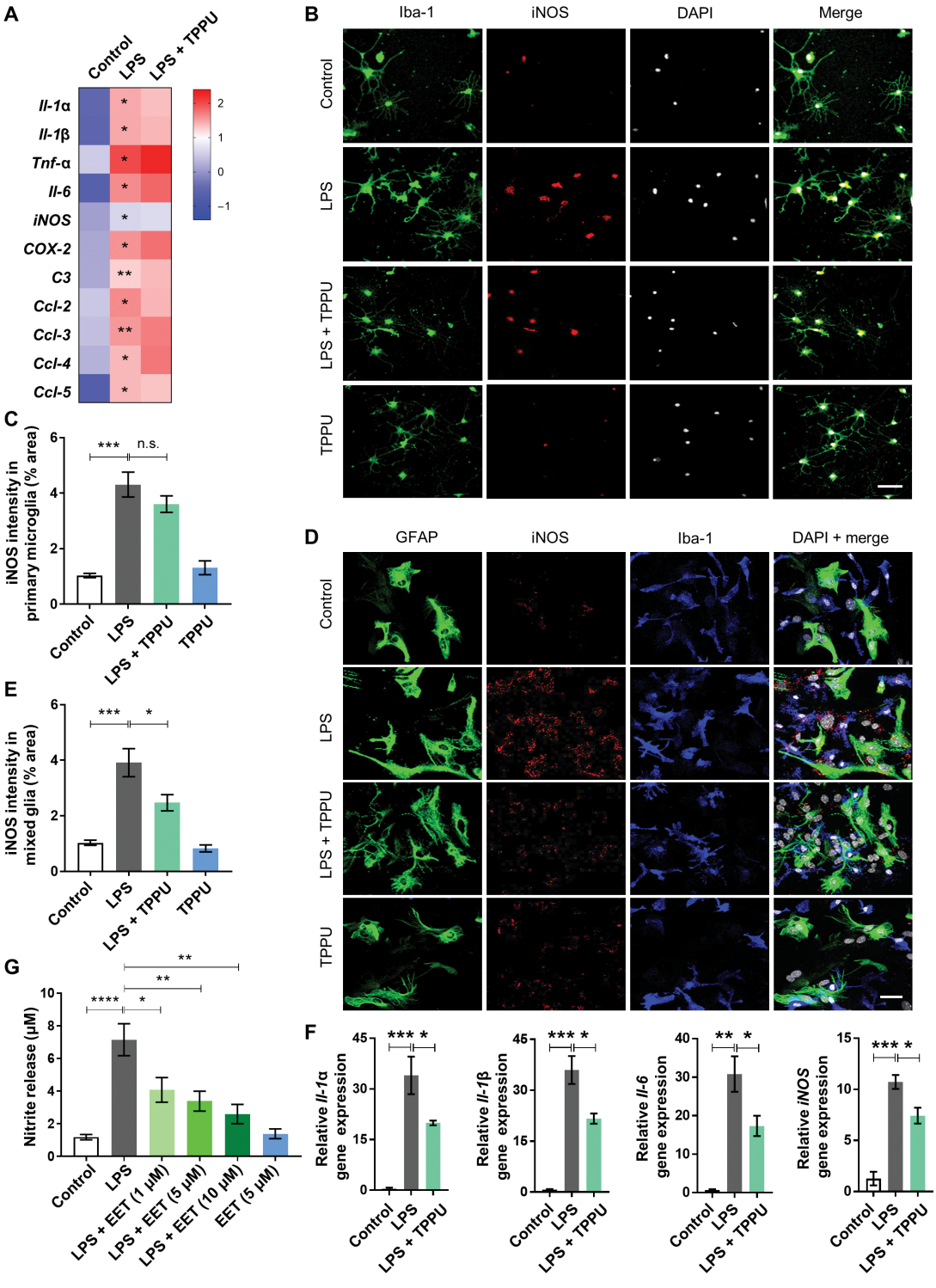

Fig. 3. TPPU and EET suppress microglial reactivity through astrocyte-microglia cross-talk. (**A**) Heatmap of qPCR analysis of inflammatory gene expression in cultured mouse primary microglia treated with vehicle (control), LPS (100 ng/ml), or LPS with a pretreatment of 10 μM TPPU (LPS and TPPU). The asterisks in the LPS column represent the comparison between control and LPS. LPS versus LPS and TPPU: nonsignificant for all genes. (**B**) Immunocytochemistry for expression of Iba-1 (green) and iNOS (red) in mouse primary microglia treated with vehicle (control), LPS, LPS and TPPU, or TPPU alone. DAPI stains the nucleus in the merged panel. (**C**) Quantification of iNOS staining intensity in (B). (**D**) Immunofluorescence staining for expression of GFAP (green), iNOS (red), and Iba-1 (blue) in mixed mouse glia cultures treated with vehicle (control), LPS, LPS and TPPU, or TPPU alone. DAPI stains the nucleus in the merged panel. (**E**) Quantification of iNOS staining intensity in (D). (**F**) qPCR analysis of mRNA expression of *Il-1α*, *Il-1β*, *Il-6*, and *iNOS* in mixed mouse glia cultures. (**G**) Nitrite concentrations measured by the Griess assay in conditioned media from mouse primary microglia cultures are shown. Data are means ± SEM of three independent experiments. ****$P < 0.0001$, ***$P < 0.001$, **$P < 0.01$, and *$P < 0.05$; n.s., not significant. Data were analyzed by one-way ANOVA with Tukey's multiple comparison test. Scale bars, 75 μm.

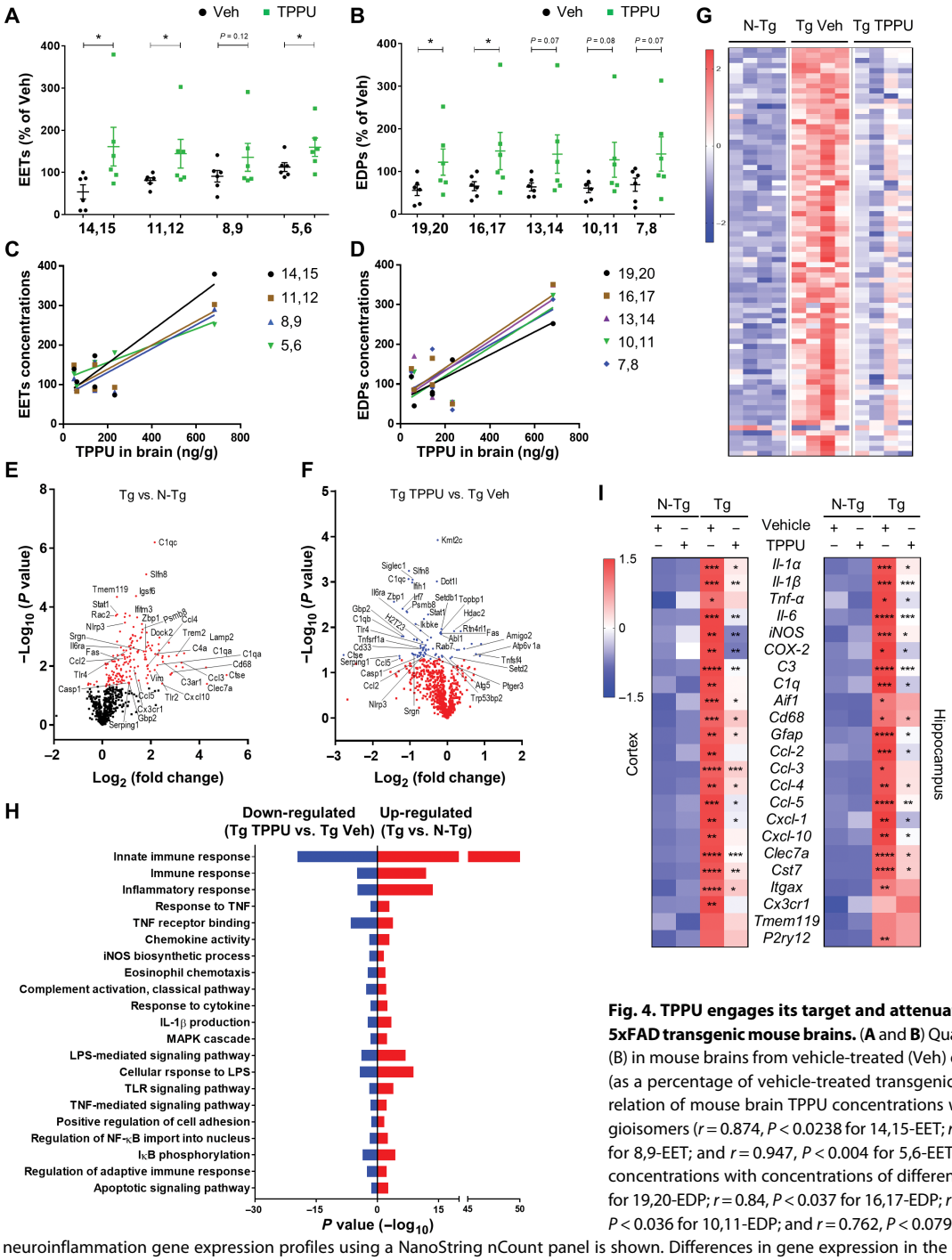

Fig. 4. TPPU engages its target and attenuates inflammatory gene expression in 5xFAD transgenic mouse brains. (**A** and **B**) Quantification of relevant EETs (A) and EDPs (B) in mouse brains from vehicle-treated (Veh) or TPPU-treated 5xFAD transgenic mice (as a percentage of vehicle-treated transgenic mouse brain concentrations). (**C**) Correlation of mouse brain TPPU concentrations with concentrations of different EET regioisomers ($r = 0.874$, $P < 0.0238$ for 14,15-EET; $r = 0.866$, $P < 0.026$ for 11,12-EET; $r = 0.02$ for 8,9-EET; and $r = 0.947$, $P < 0.004$ for 5,6-EET). (**D**) Correlation of mouse brain TPPU concentrations with concentrations of different EDP regioisomers ($r = 0.899$, $P < 0.015$ for 19,20-EDP; $r = 0.84$, $P < 0.037$ for 16,17-EDP; $r = 0.796$, $P < 0.581$ for 13,14-EDP; $r = 0.84$, $P < 0.036$ for 10,11-EDP; and $r = 0.762$, $P < 0.079$ for 7,8-EDP). (**E** and **F**) A volcano plot of neuroinflammation gene expression profiles using a NanoString nCount panel is shown. Differences in gene expression in the mouse hippocampus were stratified as follows: (E) 5xFAD transgenic versus nontransgenic mice and (F) 5xFAD transgenic mice treated with TPPU compared to 5xFAD transgenic mice treated with vehicle. For each plot, significance is plotted against fold change ($\log_2$ values). Red dots and blue dots denote genes with adjusted significance of $P < 0.05$. (**G**) A heatmap of relative expression of inflammatory pathway genes in nontransgenic mice and in transgenic mice treated with vehicle or TPPU is shown. (**H**) Gene ontology (GO) and pathway analysis of differentially expressed genes in (G) is shown, with identification of significant GO terms (biological processes) associated with differentially expressed genes. The vertical axis represents the GO category, and the horizontal axis represents the P value ($-\log_{10}$) of the significant GO terms. Red bars represent significantly up-regulated inflammatory pathways in transgenic mice versus nontransgenic mice, and blue bars represent significantly down-regulated inflammatory pathways in transgenic mice treated with TPPU versus vehicle. MAPK, mitogen-activated protein kinase; TLR, Toll-like receptor; IκB, inhibitor of NF-κB. (**I**) Heatmap shows qPCR analysis of mRNA expression in mouse cortex (left) and hippocampus (right). Asterisks in transgenic vehicle (+) TPPU (−) column represent significant changes compared to nontransgenic vehicle (+) TPPU (−). Asterisks in transgenic vehicle (−) TPPU (+) column represent significant changes compared to transgenic vehicle (+) TPPU (−). Data are means ± SEM of either six to eight mice of mixed gender (A to D) or four male mice (E to H) per group. Data were analyzed by Student's t test (A and B) or by two-way ANOVA with Bonferroni's multiple comparison test (I). For (C) and (D), correlation coefficients (r) were computed using Pearson correlations, and each dot represents an individual mouse and linear regression line.

transgenic mice compared to the vehicle-treated control transgenic mouse group. The trending, but not statistically significant, increases of some of the regioisomers of EETs and EDPs could be attributed to the differences in drug uptake or responses among individual animals. Plotting the coexpression relationship between EpFA regioisomers and TPPU indicated positive correlations between these two factors in the brain (Fig. 4, C and D), strengthening the notion that TPPU penetrated the mouse brain and antagonized its target sEH.

TPPU treatment reverses immune pathway dysregulation in 5xFAD transgenic mice

Having established the efficacy of TPPU, we tested its effects in 5xFAD mice using molecular, biochemical, neuropathological, and functional approaches (fig. S10A). To investigate the molecular mechanisms, we performed multiplex gene expression analysis using a NanoString nCounter panel enriched for inflammatory genes. We quantified the expression of 757 genes in the hippocampi of 4.5-month-old nontransgenic and transgenic mice treated with vehicle or TPPU ($n = 4$ per group). A volcano plot representation of gene expression stratified by vehicle-treated transgenic versus nontransgenic mouse groups (Fig. 4E) demonstrated the up-regulation of 171 genes (red dots) in transgenic mice. For each dot, significance was plotted against fold change ($\log_2$ values). Treatment with TPPU for 2.5 months resulted in down-regulation of 73 inflammatory genes (blue dots) in the TPPU-treated compared to the untreated transgenic mouse groups (Fig. 4F). Heatmap analysis of the 73-gene inflammatory group for individual animals demonstrated that increased inflammatory gene expression was down-regulated by TPPU treatment compared to vehicle treatment in 5xFAD transgenic mice (Fig. 4G). Next, we performed gene ontology (GO) enrichment analysis to gain further insights into the biological functions of differentially expressed genes. Our results showed that 64 pathways were significantly enriched for the identified differentially expressed genes ($P < 0.05$) (Fig. 4H). Differentially expressed genes between transgenic and nontransgenic mice were mainly enriched in immune-related processes, such as immune responses, inflammatory responses, chemokine responses, cytokine-mediated signaling, the iNOS biosynthetic pathway, the complement activation pathway, the LPS-mediated signaling pathway, cell adhesion and chemotaxis pathways, NF-κB–mediated signaling, and apoptotic signaling pathways (Fig. 4H). The majority of the inflammatory pathways up-regulated in vehicle-treated transgenic mice were down-regulated after TPPU treatment of transgenic mice (Fig. 4H). The NanoString nCounter panel results were further validated by qPCR analysis of selected proinflammatory molecules using both cortex and hippocampal tissues obtained from 5xFAD transgenic mice treated with vehicle or TPPU (Fig. 4I).

In line with the gene expression data, Western blot analysis documented elevated inflammatory markers (iNOS and COX-2) and glial cell (GFAP and Iba-1) markers in the brains of 5xFAD transgenic mice compared to nontransgenic control animals in both hippocampus (Fig. 5, A and B) and cortex (fig. S11). TPPU treatment (2.5 months) resulted in down-regulation of these marker proteins (Fig. 5, A and B, and fig. S11) and p38 mitogen-activated protein kinase previously shown to be subject to regulation by EET (*42*). These results were further validated by immunofluorescence staining for Iba-1 (Fig. 5C) and GFAP (Fig. 5D) and costaining with COX-2 and iNOS followed by quantification (Fig. 5E). Together, the findings suggest that inhibition of sEH by TPPU was effective at reversing the dysregulated immune pathways and glia reactivity in 5xFAD transgenic mice.

TPPU ameliorates Aβ pathology and cognitive impairment in 5xFAD mice

Having demonstrated a potential role for TPPU in reversing AD-associated immune system dysfunction, we then asked whether sEH inhibition by TPPU could influence Aβ pathology. We stained brain sections from 4.5-month-old and 6.5-month-old 5xFAD transgenic mice treated with vehicle or TPPU with the 6E10 antibody that recognizes the first 16 amino acids of the Aβ sequence and quantified Aβ plaque pathology in the hippocampus (Fig. 6) and cortex (fig. S12). We observed modest 6E10-positive Aβ plaque deposition in 4.5-month-old 5xFAD transgenic mice treated with vehicle (Fig. 6A), which became more severe at 6.5 months of age (Fig. 6C). TPPU treatment led to reductions in the number and size of Aβ plaques and in 6E10 antibody staining intensity in both the 4.5-month (Fig. 6B) and the 6.5-month (Fig. 6D) age groups. Characterization of glial cells surrounding the plaques using general astrocyte (GFAP) and microglia (Iba-1) markers, as well as a phagocytic microglia marker (CD68) and a neurodegenerative glia marker (Clec7a) (*43*), revealed reduced numbers of microglia per Aβ plaque (Fig. 6, E and F). These changes could have been due to reductions in amyloid plaque size because the ratio of GFAP/6E10 or Iba-1/6E10 staining intensities was comparable between vehicle-treated and TPPU-treated groups (fig. S12A). Similar results were obtained when 4.5-month-old mouse cortical samples (fig. S12, B and C) or 6.5-month-old mouse hippocampal samples (fig. S13) were analyzed.

To address whether the reduced Aβ pathology may have been caused by a possible off-target effect of TPPU on APP processing and Aβ metabolism, we performed biochemical characterizations of APP and APP-processing enzymes, including β-site APP cleaving enzyme 1 (BACE1) and the γ-secretase complex [composed of Nicastrin, Presenilin enhancer 2 (PEN2), Presenilin-1 (PS1), or PS2] (Fig. 6G). Two APP antibodies were used: the human-specific 6E10 antibody (hAPP) and a C-terminal antibody that recognizes both mouse and human full-length APP (APP-FL) and the APP C-terminal fragment (CTF). No appreciable differences were detected between vehicle-treated and TPPU-treated 5xFAD transgenic mouse groups (Fig. 6H). The same results were obtained by qPCR analysis of *App*, *Adam10*, and the Aβ-degrading enzymes *Ide* and *Klk7* in both the mouse cortex and hippocampus (fig. S14). These results argued against an off-target effect of TPPU.

Having demonstrated a prominent role of TPPU in attenuating neuroinflammation and amyloid pathology, we next assessed the brain neuronal phenotypes after long-term TPPU treatment. We chose 6.5-month-old 5xFAD transgenic mice with 4.5 months of TPPU treatment for analysis because synapse and neuronal loss could be readily detected in these mice at that age (*44*–*47*). Coimmunostaining of the presynaptic protein synaptophysin with the neuronal marker NeuN and comparison of nontransgenic or transgenic mice treated with vehicle or TPPU revealed reduced synaptophysin intensity in area CA3 of the hippocampus in transgenic mice compared to nontransgenic controls (Fig. 7, A and B). TPPU treatment partially elevated synaptophysin expression in transgenic mouse brains compared to the brains of mice treated with vehicle control (Fig. 7, A and B). Double immunostaining for synaptophysin and postsynaptic density protein 95 (PSD95) followed by high-resolution imaging and quantification showed diminished synaptophysin/PSD95-positive synaptic puncta in 5xFAD mice, which was rescued by TPPU treatment (Fig. 7, C and D). Measurement of NeuN-positive neurons in different brain areas including the subiculum, layer V of cortex,

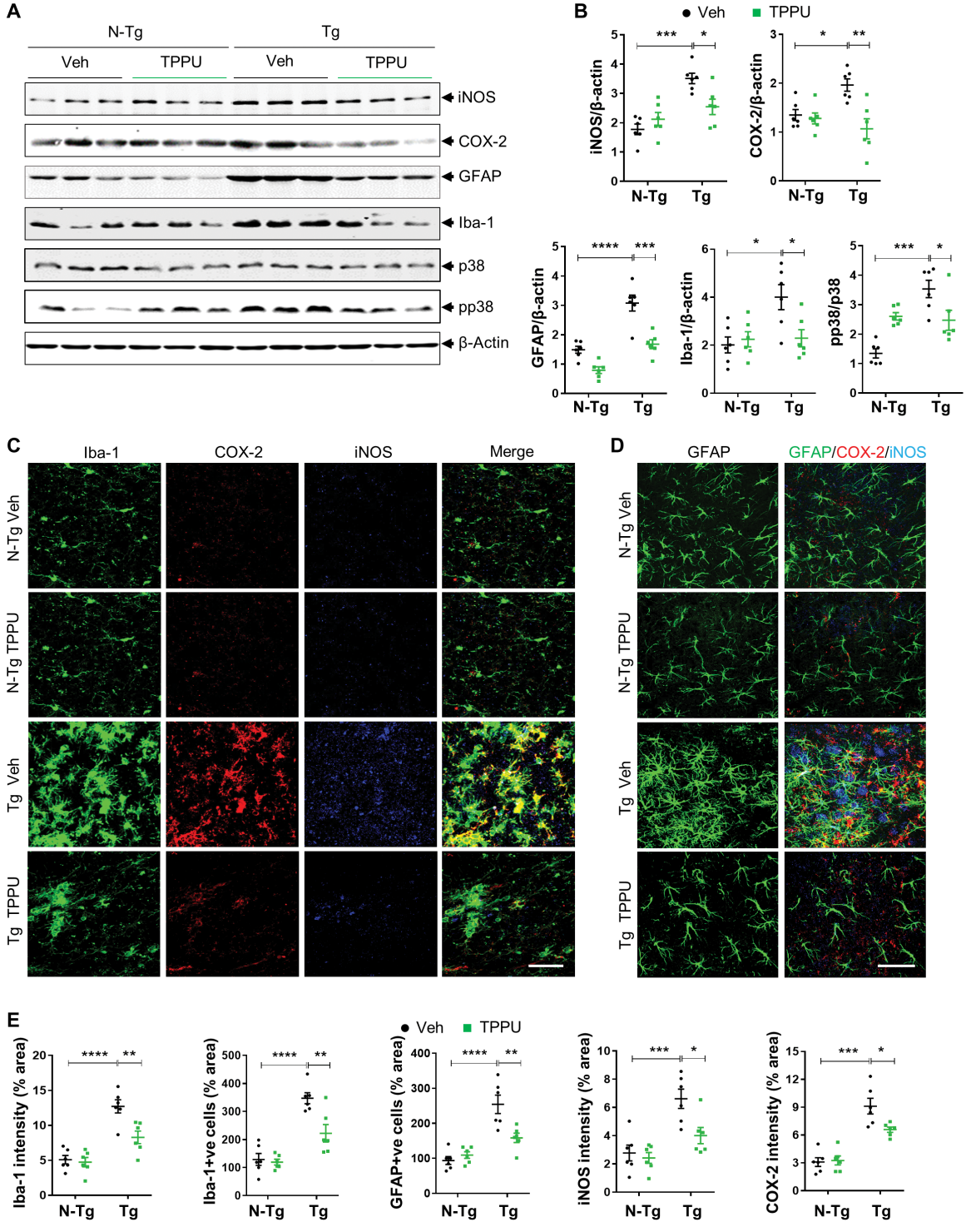

Fig. 5. TPPU reduces neuroinflammatory markers and gliosis in 5xFAD transgenic mouse brains. (**A**) Representative Western blot of expression of iNOS, COX-2, GFAP, Iba-1, total p38, and phosphorylated p38 (pp38) in hippocampal samples from nontransgenic mice and 5xFAD transgenic mice treated with vehicle or TPPU starting at 2 months of age for 2.5 months. β-Actin was used as a loading control. (**B**) Quantification of Western blot in (A). (**C**) Triple immunofluorescence staining for the expression of Iba-1 (green), COX-2 (red), and iNOS (blue) in the hippocampus of nontransgenic mice and 5xFAD transgenic mice treated with vehicle or TPPU starting at 2 months of age for 2.5 months. (**D**) Immunofluorescence staining for GFAP alone (left) and a merged panel for GFAP (green), COX-2 (red), and iNOS (blue) staining (right) for hippocampal sections from nontransgenic mice and 5xFAD transgenic mice treated with vehicle or TPPU starting at 2 months of age for 2.5 months. (**E**) Quantification of Iba-1, iNOS, and COX-2 staining intensities and the number of Iba-1–positive and GFAP-positive cells in the hippocampus is shown. Data are means ± SEM of six to eight mice per group of mixed gender. ****$P < 0.0001$, ***$P < 0.001$, **$P < 0.01$, and *$P < 0.05$. Data were analyzed by two-way ANOVA with Bonferroni's multiple comparison test. Scale bars, 50 μm.

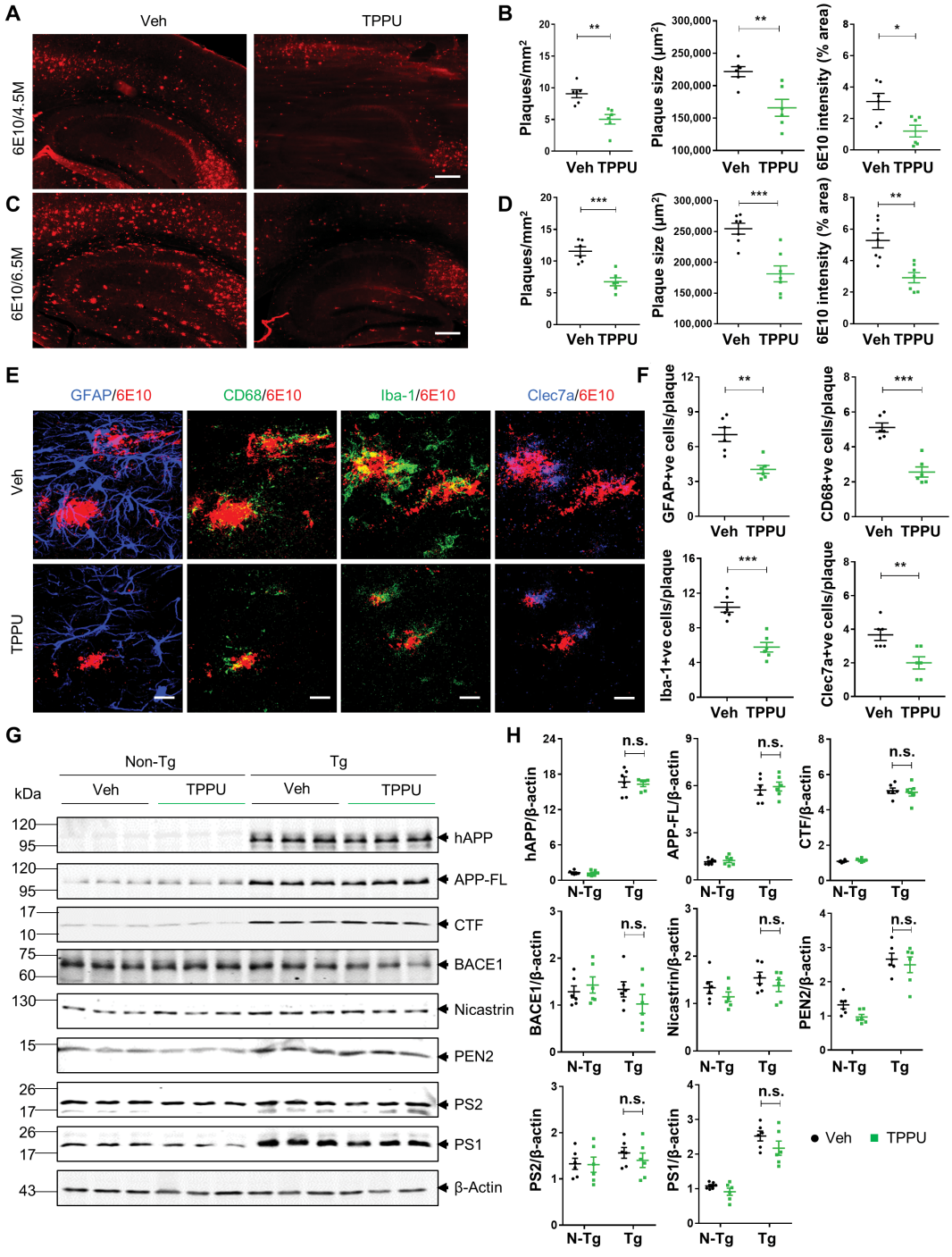

Fig. 6. TPPU reduces Aβ burden but does not alter APP processing in 5xFAD transgenic mouse brains. (**A**) Immunohistochemistry with the 6E10 antibody in mouse brains from 4.5-month-old 5xFAD transgenic mice treated with vehicle or TPPU for 2.5 months. (**B**) Quantification of amyloid plaques/mm^2 area, amyloid plaque size (μm^2), and 6E10 staining intensity from (A). (**C**) Immunohistochemistry with the 6E10 antibody in mouse brains from 6.5-month-old 5xFAD transgenic mice treated with vehicle or TPPU for 4.5 months. (**D**) Quantification of amyloid plaques/mm^2 area, amyloid plaque size (μm^2), and 6E10 staining intensity from (C). (**E**) Representative double immunofluorescence images of the hippocampus of 4.5-month-old 5xFAD transgenic mice treated with vehicle or TPPU. Images show staining for GFAP (blue) and 6E10 antibody (red), CD68 (green) and 6E10 antibody (red), Iba-1 (green) and 6E10 antibody (red), and Clec7a (blue) and 6E10 antibody (red). (**F**) Quantification of GFAP-positive cells, CD68-positive cells, Iba-1–positive cells, and Clec7a-positive cells within a 100-μm radius of an amyloid plaque (86 to 123 plaques per group were counted) in (E). (**G**) Representative Western blot of expression of hAPP, APP-FL, CTF, BACE1, Nicastrin, PEN2, PS2, and PS1 in hippocampal samples from 4.5-month-old nontransgenic and 5xFAD transgenic mice treated with vehicle or TPPU. β-Actin was used as a loading control. (**H**) Scatter dot plot shows mean protein expression compared to β-actin from (G). Each dot represents normalized protein expression data for one mouse. Data are means ± SEM of six to eight mice per group of mixed gender. ***$P < 0.001$, **$P < 0.01$, and *$P < 0.05$; N.S., not significant. Data were analyzed by either Student's *t* test (B, D, and F) or by two-way ANOVA with Bonferroni's multiple comparison test (H). Scale bars, 400 μm (A and C) and 100 μm (E).

and the hippocampal CA3 region all showed different degrees of neuronal loss in the 5xFAD transgenic mice and partial rescue by TPPU treatment (Fig. 7E and fig. S15A). Expression of neuronal and synaptic markers correlated with synaptic plasticity measured by long-term potentiation (LTP) recordings of the Schaffer collateral pathway of the hippocampus (Fig. 7, F and G).

Synaptophysin and NeuN double immunostaining of brain sections from 4.5-month-old 5xFAD transgenic mice revealed that reduced synaptophysin immunoreactivity was observed at this age although the number of NeuN-positive neurons remained unchanged (fig. S15, B to D). Given that increased synaptophysin staining intensity could be detected after TPPU treatment (fig. S15C), we wondered whether this was associated with functional improvement at this age. We thus evaluated the effect of TPPU treatment on cognition using the novel object recognition test (Fig. 7H) and a fear conditioning paradigm (Fig. 7I). The novel object recognition test assesses hippocampus-dependent long-term recognition memory by calculating the percent time spent with a novel object [the object discrimination

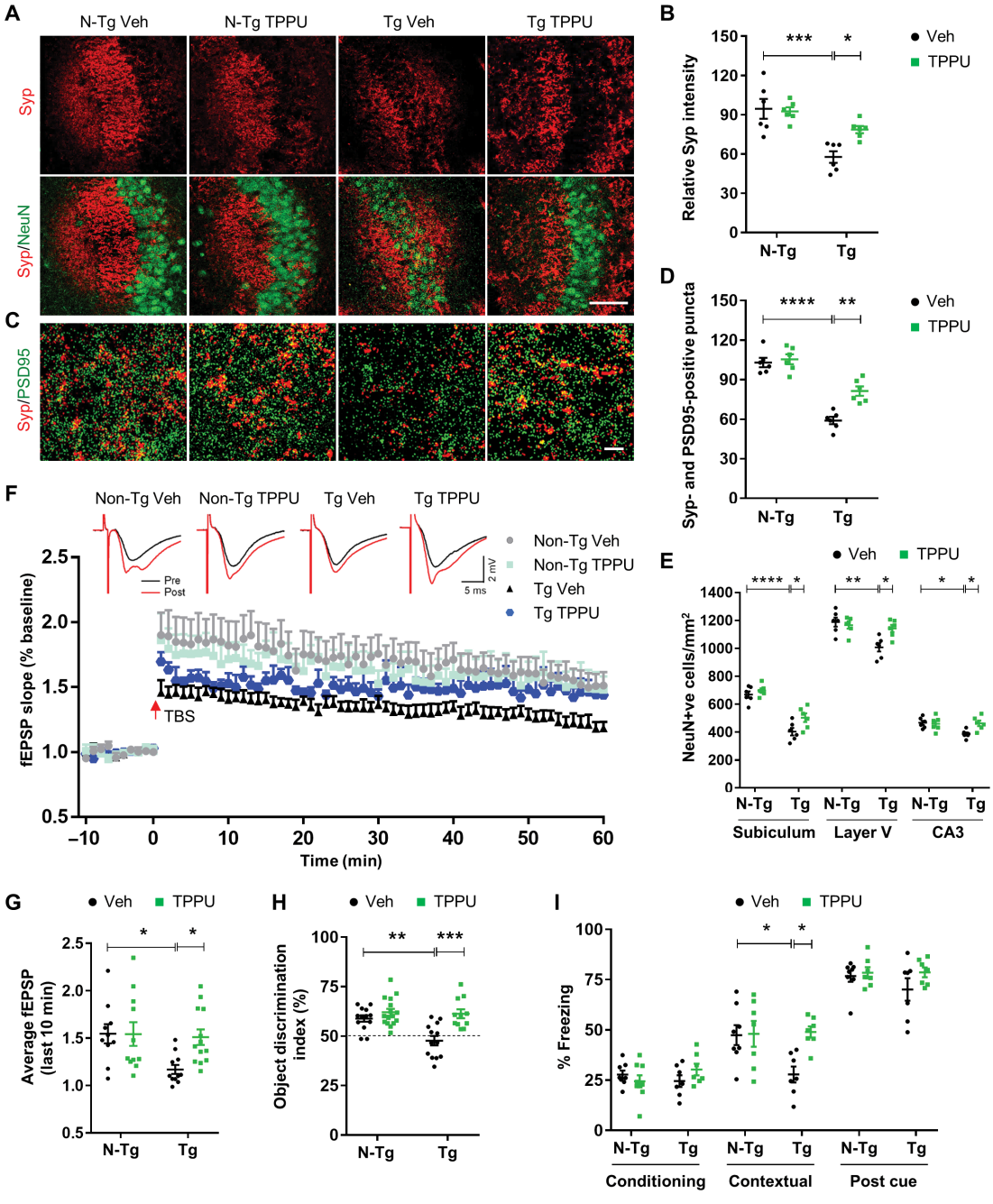

Fig. 7. TPPU ameliorates synaptic deficits and cognitive function in 5xFAD transgenic mice. (**A**) Representative images of co-immunostaining for synaptophysin (Syp) and NeuN in hippocampal CA3 sections from 6.5-month-old nontransgenic and 5xFAD transgenic mice treated with vehicle or TPPU. (**B**) Quantification of relative synaptophysin staining intensity (% area) in (A). (**C**) High-resolution images of coimmunostaining for synaptophysin and PSD95 in hippocampal CA3 sections from 6.5-month-old nontransgenic and 5xFAD transgenic mice treated with vehicle or TPPU. (**D**) Quantification of synaptophysin and PSD95 double-positive puncta (% nontransgenic mice treated with vehicle) in (C). (**E**) Quantification of NeuN-positive cells in subiculum, layer V of cortex, and hippocampal CA3 of 6.5-month-old nontransgenic and 5xFAD transgenic mice treated with vehicle or TPPU. (**F**) Slope of the field excitatory postsynaptic potential (fEPSP) in response to theta burst stimulation delivered to the Schaffer collateral pathway of 6.5-month-old nontransgenic and 5xFAD transgenic mice treated with vehicle or TPPU. Top: fEPSP traces before (black) or after (red) theta burst stimulation are shown. Calibration was 2 mV, 5 ms. (**G**) Average fEPSP slope in the last 10 min of theta burst stimulation. (**H**) Results of the novel object recognition test displayed as the object discrimination index for 4.5-month-old nontransgenic and 5xFAD transgenic mice treated with vehicle or TPPU for 2.5 months. The dashed line represents a 50% chance of random object exploration. (**I**) Results of a fear conditioning test for 4.5-month-old nontransgenic and 5xFAD transgenic mice treated with vehicle or TPPU for 2.5 months. The percent of mice showing a freezing response in the fear conditioning test is displayed for the conditioning arm (left), contextual arm (center), and post-cued arm (right). Values are expressed as means ± SEM of 6 to 9 mice per group (A to E), 10 to 13 sections from 5 to 6 animals per group (F and G), or 12 to 16 mice per group (H and I). All mouse groups were mixed gender. Data were analyzed by two-way ANOVA with Bonferroni's multiple comparison test. ***$P < 0.001$, **$P < 0.01$, and *$P < 0.05$. Scale bar, 200 μm (A) and 30 μm (C).

index (ODI)]. The vehicle-treated 5xFAD mice displayed a decreased ODI average, which was elevated upon TPPU treatment (Fig. 7H). We further performed fear conditioning to test hippocampal-dependent (contextual test) and hippocampal-independent (cued test) associative learning (Fig. 7I). The four groups tested exhibited no differences in freezing percentage during the conditioning phase. During the contextual test, vehicle-treated 5xFAD transgenic mice displayed a decreased freezing percentage compared to nontransgenic mice, suggesting an impaired contextual memory. Comparatively, the TPPU-treated 5xFAD transgenic mouse group exhibited an increase in freezing frequency compared to the vehicle-treated transgenic mouse group. In addition, the percentage of freezing after the cue

was presented in the cued test was similar between the mouse groups. Thus, the 5xFAD transgenic mice exhibited specific impairment in the hippocampus-dependent contextual fear conditioning test, and this phenotype was improved after TPPU treatment. Together, these results demonstrate that TPPU treatment rescued synaptic deficits and memory and cognitive behaviors in 5xFAD transgenic mice.

DISCUSSION

Using postmortem human brain samples, primary cell cultures, and two AD (5xFAD and APP^{NLGF} knock-in) mouse models, we investigated the role of sEH in neuroinflammation and AD pathogenesis and tested the therapeutic effect of an orally bioavailable small-molecule sEH inhibitor, TPPU. We found that the amount of sEH was elevated in human AD postmortem brains and Aβ mouse models of AD. Increased sEH in 5xFAD transgenic mice correlated with lower amounts of EETs and EDPs. Preadministration of EET or TPPU prevented acute LPS-induced neuroinflammation in cultured mouse astrocytes and mice. Long-term TPPU treatment at the onset of AD neuropathology was able to reverse microglia and astrocyte activation and immune pathway dysregulation at the molecular, cellular, and functional levels, and these changes were associated with attenuated Aβ pathology and improved synaptic and cognitive function. Moreover, TPPU treatment reinstated expression of and positively correlated with EpFAs in the 5xFAD transgenic mouse brain, supporting the brain penetration and target engagement of TPPU.

Our results demonstrate that sEH was not only elevated in AD mouse models but also was increased in human AD postmortem brains. Similar increases in sEH have also been reported in APP/PS1 AD mice in which genetic ablation of *Ephx2* was shown to ameliorate Aβ pathology and behavioral deficits (*29*). Whereas these aspects were consistent between our study and that of Lee *et al.* (*29*), there were noticeable differences. Specifically, Lee *et al.* (*29*) reported increased GFAP reactivity and altered APP/Aβ dynamics when *Ephx2* was deleted in APP/PS1 AD mice, whereas we detected reduced astrogliosis with no change in APP expression or processing upon TPPU treatment. Although the precise reason for the discrepancies is not clear, it is important to note that our approach involved pharmacological treatment of adult mice. In contrast, Lee *et al.* (*29*) used genetic knockout mice in which *Ephx2* was deleted throughout life. Critically, sEH contains a C-terminal hydrolase and an N-terminal phosphatase domain. *Ephx2* deletion ablated both activities, whereas TPPU and other sEH inhibitors only inactivated the hydrolase activity. In this regard, the Arg287Gln and Lys55Arg polymorphisms of sEH are associated with reduced phosphatase activity and increased risk for coronary heart disease and type 2 diabetes (*48*–*51*), suggesting a protective role of the sEH phosphatase domain. Thus, it is tempting to speculate that the increased astrogliosis and altered APP/Aβ pathway dynamics reported by Lee *et al.* (*29*) may have been due to the loss of the sEH phosphatase activity.

Our cell type–specific analysis demonstrated that mouse astrocytes were the predominant cells expressing sEH where it was deregulated under AD conditions. This led to diminished EETs and EDPs and a reduction in their anti-inflammatory activities in both astrocytes and microglia. Besides the astrocytes, sEH is known to be highly expressed in the vasculature where it mediates vascular inflammation and barrier function through both EETs and EDPs (*20*, *52*). Our expression analysis of sorted vascular endothelial cells revealed no appreciable differences in *Ephx2* expression between 5xFAD transgenic mice and nontransgenic controls, arguing against a major contribution of vascular sEH in disease pathogenesis. Nevertheless, it remains possible that the overall therapeutic effect of TPPU was due to its inhibition of sEH in both astrocytes and vascular endothelium and possibly other cell types as well. A recent report showed that liver sEH modulates depressive-like behaviors in mice, suggesting that sEH expressed in the peripheral system could influence brain function (*53*). Hence, although our finding that TPPU entered the mouse brain and correlated with an increase in EETs and EDPs supported a CNS-intrinsic mechanism, we cannot exclude the possibility that TPPU could also have exerted its effects through the inhibition of liver sEH. The creation of mice with tissue-specific knockout of *Ephx2* in astrocytes or liver is needed to address the cell type–specific effects of TPPU (*53*).

Our NanoString nCount panel analysis followed by qPCR validation revealed that multiple immune and inflammatory response pathways were up-regulated in the 5xFAD transgenic mice and down-regulated by TPPU treatment. In addition, recent reports have identified a signaling pathway whereby microglia-mediated neuroinflammation [in a C1q-, interleukin-1α (IL-1α)–, and TNF-dependent manner] induced expression of A1 astrocyte genes that were toxic to neurons (*54*–*56*). Our gene expression analysis revealed that a number of A1 astrocyte genes (*Serping1*, *Gbp2*, *Srgn*, *H2T23*, and *Psmb8*) were normalized by TPPU treatment, suggesting that TPPU may reduce neuroinflammation by mitigating astrocyte activation, thus promoting neuronal survival. In addition, NOD-, LRR- and pyrin domain-containing protein 3 (NLRP3) inflammasome activation has been implicated in producing harmful chronic inflammatory reactions and impairing microglial Aβ clearance and cognitive function in AD (*8*, *57*, *58*). We found that *Nlrp3* and *Casp1* were both up-regulated in 5xFAD transgenic mouse brains and down-regulated by TPPU treatment. Therefore, TPPU could suppress chronic neuroinflammation through NLRP3-dependent mechanisms.

We demonstrate here that long-term TPPU treatment not only dampened glia reactivity but also ameliorated Aβ pathology and improved functional outcomes in 5xFAD transgenic mice. Ample evidence documents that prolonged microglia activation leads to impaired Aβ phagocytosis and triggers the production of proinflammatory mediators and that its inhibition reverses these anomalies (*59*, *60*). Therefore, the observed reduction of Aβ pathology and improvement of neuronal function that we observed after TPPU treatment could be the consequences of glia normalization. In addition, microglia, through complement-dependent mechanisms, have been shown to mediate synapse elimination (*61*, *62*). Our gene expression analysis revealed that aberrant *C1q* and *C3* up-regulation in 5xFAD transgenic mice was rescued by TPPU treatment (Fig. 4), and this correlated with increased synaptophysin and PSD95-positive synaptic puncta in the hippocampus (Fig. 7). Thus, the improved synaptic plasticity and behavioral performance in TPPU-treated 5xFAD transgenic mice could be attributed directly to TPPU by blocking complement-mediated synapse loss, which should be investigated in future experiments.

There are several limitations to our study. First, the precise mode of action, in particular, whether TPPU's effect could be solely attributed to EET stabilization and how EETs mediate different biological functions, awaits further investigation. Second, we started the TPPU treatment at an early stage before the development of frank pathology. Whether TPPU remained effective when administered at later times after amyloid pathology was already established was not addressed. Third, our results were obtained using 5xFAD transgenic mice with

numerous artificial features, including transgene overexpression and fast and aggressive Aβ pathology development. These caveats need to be taken into consideration when interpreting the results. Similar to all animal model studies, whether our findings can be recapitulated in humans requires further testing.

Several classes of sEH inhibitors have been developed (*63*). Overall, they are well tolerated in preclinical studies, establishing a large safety window for targeting of sEH. Among these, TPPU is widely used as a tool compound because of its superior potency, specificity, and pharmacokinetics (*31*, *64*–*67*). We report here that long-term administration of TPPU resulted in retention in the mouse brain where it engaged its sEH target and afforded beneficial effects in a mouse model of AD. These features make TPPU an attractive candidate for further development as a potential treatment for AD.

MATERIALS AND METHODS

Study design

The goal of this study was to establish evidence in the 5xFAD transgenic mouse model of AD that inhibition of the sEH with the small-molecule inhibitor TPPU could modify amyloid pathology in the mouse brain. The C57BL/6 and 5xFAD mice were obtained from the Jackson laboratory (Bar Harbor, ME). APP^{NLGF} mice were obtained from RIKEN (*33*). Mice were housed four to five per cage in a pathogen-free mouse facility with ad libitum access to food and water on a 12-hour light/dark cycle. Male and female mice at about equal ratios were used for all experiments except for NanoString nCount panel experiments. Only male mice were used to achieve within-group consistency for better cross-group comparisons.

The C57BL/6 wild-type mice were used to investigate the acute anti-inflammatory effects of the sEH inhibitors TPPU and EC5026. To determine the chronic long-term effects of TPPU on mitigating neuroinflammation, amyloid plaque pathology, synaptic abnormalities, and behavioral deficits, 5xFAD transgenic mice were used. The APP^{NLGF} knock-in mice were used only to determine changes in sEH protein expression. For mouse experiments, one individual would randomize the animals, plates, and slides, and another would analyze them. The minimum sample size for all experiments was held at six mice per group based on the design of previous studies (*11*). To improve our power, and thus our ability to statistically detect smaller effects, many of our analyses included more mice per group. In particular, 12 to 16 mice per experimental group were used for behavioral tests, and 6 to 9 mice per experimental group were randomly selected for biochemical analysis. All procedures were performed in accordance with National Institutes of Health (NIH) guidelines and approval of the Baylor College of Medicine Institutional Animal Care and Use Committee. All in vitro experiments were performed at least twice, each with at least three technical replicates.

Postmortem brain tissues from patients with AD and nondemented controls were provided by the University of Pennsylvania Center for Neurodegenerative Disease Research. Informed consent had been obtained from all participants for the use of their postmortem tissues. The AD patient and control demographic data can be found in table S2. Influence of gender on the study results was not analyzed because of the small sample size.

TPPU and EC5026 treatment

The sEH inhibitors TPPU was synthesized as described previously (*31*), and EC5026 was synthesized as described (international patent publication no. WO 2015/148954 A1). TPPU or EC5026 was dissolved either in dimethyl sulfoxide for in vitro and ex vivo treatment (TPPU only) or in 1% polyethylene glycol, molecular weight 400 (PEG-400, Thermo Fisher Scientific) for in vivo treatment. The vehicle mice received oral gavage treatment of 1% PEG-400. Mice were perfused with saline before collecting brain for biochemical analysis. In the acute TPPU or EC5026 treatment regimen, 10- to 12-week-old C57BL/6 mice received first dose of TPPU (3 mg/kg) via oral gavage 24 hours before cotreatment of LPS (3 mg/kg, i.p.) and TPPU or EC5026 (second dose). Eighteen hours after cotreatment, mice were euthanized for analysis.

For long-term TPPU treatment, 5xFAD transgenic mice received TPPU (3 mg/kg) in drinking water for either 2.5 or 4.5 months starting at 2 months of age. The vehicle mice received 1% PEG-400 in drinking water. Every 2 weeks, mice were supplied with a new water bottle containing fresh TPPU or vehicle solution.

Microglia and astrocyte monocultures and mixed culture

Primary glia cultures were prepared as described previously (*61*). Briefly, mouse cortices and hippocampi were isolated from newborn pups (P0 and P1) in dissection medium [Hanks' balanced salt solution (HBSS) with 10 mM Hepes and 1% (v/v) penicillin/streptomycin] and cut into small pieces. Tissue was digested with 2.5% trypsin at 37°C for 15 min before trypsin inhibitor (1 mg/ml) was added. Next, tissue was centrifuged for 5 min at 1500 rpm, triturated, and resuspended in Dulbecco's modified Eagle's medium with 10% fetal bovine serum. Cells were plated onto poly-D-lysine (PDL)–coated T-75 flasks at 50,000 cells/cm^2 to generate mixed glial cultures. For astrocyte and microglia coculture, cells were trypsinized and seeded at 40,000 cells/cm^2 and cultured for 3 to 4 days in PDL-coated plates for mRNA assays or immunocytochemistry (ICC). For separation of microglia, confluent flasks were tapped on the table, and floated cells, which were mostly microglia, were collected from the media. Microglia cells were then seeded at 50,000 cells/cm^2 and cultured for another day in PDL-coated 12-well plates for mRNA assays or on coverslips for staining. After collecting microglia cells, remaining cells (mostly astrocytes) were trypsinized and seeded at 40,000 cells/cm^2 and cultured for another 2 days in PDL-coated plates for mRNA assays or ICC.

RNA extraction and expression analysis

Total RNA was extracted from cells or human or mouse brain tissues using RNeasy Mini kit (QIAGEN, 74106). Reverse transcription was carried out using iScript Reverse Transcription Supermix (Bio-Rad, 1708840). The qPCR analyses were performed using SYBR Green PCR master mix (Bio-Rad) on a CFX384 Touch Real-Time PCR Detection System. Primer sequences can be found in table S3.

For NanoString nCounter panel analysis, RNA was isolated from 4.5-month-old male mouse hippocampus, and 770 transcripts were quantified with the NanoString nCounter multiplexed target platform using the Mouse Neuroinflammation panel (www.nanostring.com). nCounts of mRNA transcripts were normalized using the geometric means of 10 housekeeping genes (*Csnk2a2*, *Ccdc127*, *Xpnpep1*, *Lars*, *Supt7l*, *Tada2b*, *Aars*, *Mto1*, *Tbp*, and *Fam104a*) and analyzed using nSolver 4.0 and the Advanced Analysis 2.0 plugin. Fold change expression and *P* values were calculated by linear regression analysis using negative binomial or log-linear models. *P* values were corrected for multiple comparisons using the Benjamini-Yekutieli method. Volcano plots of differential expression data were plotted using

the $-\log_{10}$ (P value) and $\log_2$ fold change using GraphPad Prism. GO enrichment analysis was performed using www.innatedb.com/. Heatmaps were constructed using GraphPad Prism.

Griess assay for nitrite measurement

Griess assay was performed, as described previously (*68*). Briefly, standards in triplicate were used for each plate. Standard mix was made up of 1 ml of media and 1 μl of sodium nitrite and added to wells in volumes, increasing by 5 μl from 0 to 35 μl. Media were added to each well to bring the volume up to a total of 100 μl. Sample supernatant was added in duplicate to remaining wells in 100 μl. Then, 100 μl of Griess reagent (Sigma-Aldrich) was added to each well and incubated at room temperature for 20 min. Absorbance at 540 nm was detected in a Synergy 2 Multi-Detection Microplate Reader.

Cell-type purification and fluorescence-activated cell sorter sorting

Mice were perfused with ice-cold phosphate-buffered saline (PBS); adult mouse brains (whole brain minus cerebellum) were chopped and resuspended in 2.5 ml of HBSS without Ca^{2+} and without Mg^{2+} containing activated papain and deoxyribonuclease. Cell-type purification and fluorescence-activated cell sorter (FACS) sorting were done as described (*34*). Briefly, brains were incubated at 37°C and then triturated four times with a fire-polished glass Pasteur pipette. Next, samples were mixed with $HBSS^+$ [HBSS and 0.5% bovine serum albumin (BSA), 2 mM EDTA] and centrifuged for 5 min. The pellet was resuspended in 1000 ml of $HBSS^+$ and centrifuged for 15 s at room temperature. The supernatant was collected and was filtered through a cell strainer (BD SKU 352340) and centrifuged for 5 min at 300*g* at 4°C. To remove myelin, the Miltenyi myelin removal beads were used according to the manufacturer's instructions (Miltenyi, 130-096-733). After that, cells were centrifuged at 300*g* for 5 min at 4°C. Next, the cells were resuspended in 1 ml of $HBSS^+$ solution and passed through an LS column. The total effluent was then centrifuged for 5 min at 300*g* at 4°C to pellet the cells. For the antibody staining, the cells were resuspended in $HBSS^+$ solution and then stained for with CD45-BV421 (BD, 563890), CD11b-FITC (BD, 553310) for microglia, ACSA-2-APC (Miltenyi, 130-102-315) for astrocytes, and cell viability blue fluorescent dye (Invitrogen, L23105). After FACS sorting, the cells were collected in Eppendorf tubes, centrifuged at 1500 rpm for 5 min, and resuspended in RLT buffer containing 1% β-mercaptoethanol (BME) for future qPCR analysis. The mRNA was extracted using the QIAGEN RNEasy Micro kit (QIAGEN, 74004).

Immunofluorescence staining

Cells were fixed with 4% paraformaldehyde in 1× PBS for 15 min and processed for ICC, as described previously (*69*). First, nonspecific sites were blocked with 0.2% BSA, 0.5% Triton X-100, and 0.05% Tween 20 in PBS for 1 hour at room temperature. Cells were then incubated with different primary antibodies: sEH [1:1000; Hammock laboratory (*26*)], GFAP (1:1000; Millipore), iNOS (1:500; Thermo Fisher Scientific), Iba-1 (1:1000; Wako), and COX-2 (1:1000; Thermo Fisher Scientific) at 4°C overnight. Appropriate secondary antibodies (Alexa Fluor 488, 555, or 647; Invitrogen) were used followed by incubation with 4′,6-diamidino-2-phenylindole (DAPI) to stain the nucleus. The coverslip-containing stained cells were washed twice with PBS and mounted on slides. After immunofluorescent staining, five individual areas from each coverslip were imaged using ×20 magnification under a Leica TCS confocal microscope.

For mouse brain analysis, immunohistochemistry was performed on free-floating microtome-cut sections (30 μm in thickness), as described previously (*68*). Briefly, mice brains were postfixed in 4% paraformaldehyde overnight at 4°C and transferred to 30% sucrose solution after perfusion with saline. Sections were incubated with different antibodies: sEH (1:1000) (*26*), GFAP (1:1000; Millipore), iNOS (1:250; Thermo Fisher Scientific), Iba-1 (1:800 or 1:500; Wako or Novus Biologicals, respectively), COX-2 (1:500; Thermo Fisher Scientific), CD68 (1:500; BioLegend), 6E10 (1:1000; BioLegend), synaptophysin (1:500; Abcam), PSD95 (1:200; Millipore), NeuN (1:1000; Millipore), and Clec7a (1:50; Invivogen). Appropriate secondary antibodies (Alexa Fluor 488, 594, or 647; Invitrogen) were used followed by incubation with DAPI. A total of three to four sections per brain containing the hippocampus and cortex and five to seven mice per group were stained with antibodies as mentioned above.

Image quantification

After immunofluorescence staining, confocal images were captured, and mean intensity of fluorescence, number of immunoreactive cells, and size of plaques were quantified using the ImageJ software (NIH). For quantification of 6E10 in the mouse cortex and hippocampus, sections were scanned using an EVOS FL Auto system. Images were then analyzed by ImageJ, and background was subtracted by the software for fluorescence images before quantification. For synaptic marker colocalization studies, imaging was performed with a Leica confocal microscope, using a 63× oil objective with a 4.0 digital zoom in the CA3 region. *Z*-stacks of 5-μm thickness from the middle of the tissues (to avoid staining artifacts) were obtained with a 0.2-μm step size and two frame-averaged 512 × 512 images for each channel. Because of great variation in synaptic puncta densities by brain region, care was taken to image from the same areas consistently across all samples and experiments. *Z*-stacks with dual synaptic puncta labeling were analyzed using the ImageJ software. For NeuN-positive cell quantification, eight images from each mouse (n = 6 mice in each group) were counted manually. For Aβ plaque–associated Iba-positive, CD68-positive, GFAP-positive, Clec7a-positive cell quantification, abovementioned marker-positive cells were counted within 100-μm radius of the 6E10-positive plaques. Total 86 to 123 plaques were counted in each group. Cell numbers were normalized to the plaques. All the images were captured and analyzed blindly using coded slides.

Western blotting

Cells or brain tissues were collected and resuspended in modified radioimmunoprecipitation assay buffer containing protease and phosphatase inhibitor mixture. Cell suspensions were sonicated after resuspension, whereas mouse brain tissues were homogenized, sonicated, and then centrifuged at 14,000*g* for 45 min at 4°C, as described previously (*70*). Briefly, protein concentrations were estimated using a bicinchoninic acid kit (Thermo Fisher Scientific). Lysates were separated on 7.5 to 15% SDS–polyacrylamide electrophoresis gels (Bio-Rad). After the separation, proteins were transferred to a nitrocellulose membrane, and nonspecific binding sites were blocked by treating with either Odyssey blocking buffer (LI-COR) or tris-buffered saline with 5% BSA followed by antibody incubation: sEH [1:300 or 1:1000; Santa Cruz Biotechnology or Hammock laboratory, respectively (*26*)], iNOS (1:1000; Cell Signaling Technology), GFAP (1:15,000; EMD Millipore), Iba-1 (1:1200; Wako), Cox-2 (1:500; Thermo Fisher Scientific), 6E10 (1:1000; for human APP, BioLegend), APP (1:1000; recognizes APP-FL and CTF, Cell Signaling Technology), Nicastrin (1:1000;

Cell Signaling Technology), PEN2 (1:1000; Cell Signaling Technology), BACE1 (Cell Signaling Technology), PS1 (1:1000; Cell Signaling Technology), PS2 (1:1000; Cell Signaling Technology), and β-actin (1:10,000; Sigma-Aldrich). Secondary IR-680–conjugated goat anti-mouse or goat anti-rabbit (1:10,000; Molecular Probes) and IRDye 800–conjugated donkey anti-rabbit or donkey anti-goat (1:10,000; Rockland, PA, USA) were used. Western blot images were captured with a LI-COR Odyssey machine (LI-COR). The Western blot bands were quantified using ImageJ software (NIH).

Behavioral analysis

The novel object recognition protocol included three phases: habituation phase, a training phase, and an object recognition phase. The habitation phase included one session, 5 min in length, in which the animals were allowed to freely explore a small Plexiglas arena (measuring 22 cm by 44 cm) that was used in the training and testing phase. One day after habituation, the animals underwent training. During the training phase, the animals were placed in the same arena with the addition of two identical objects. The animals were allowed to freely explore the objects for 5 min. Twenty-four hours after the training phase, the test phase was initiated. During the testing phase, the animal was placed in the same arena with one object previously explored in the training phase, the familiar object, and one novel object differing in color and shape but sharing a common size and volume. The animals were allowed to freely explore the objects for 5 min. ANY-maze software was used to measure the time spent exploring each object. Exploration of an object was defined by head orientation directed toward the object or physical contact with the object. The object discrimination ratio (ODR) was calculated by the following formula: ODR = (time exploring specified object) / (time exploring novel object + time exploring familiar object) × 100. The fear conditioning protocol involved a training phase, context test, and a cued test as previously described (*71*). During the training phase, the mice were placed in the training chamber and allowed to freely explore the environment. At 3 min, an 80-dB white noise was presented as auditory conditioned stimulus for 30 s. During the last 2 s of the auditory stimulus, the unconditioned stimulus, a foot shock (0.8 mA, 2 s), was administered. The conditioned stimulus and unconditioned stimulus were then presented a second time at the 5-min mark of the training procedure. After the second presentation of the unconditioned stimulus, the mice stayed in the training chamber for an additional 2 min without additional stimulation. The animals were returned to their original housing cages. Twenty-four hours after the training procedure, the context test was performed. The mice were returned to the same training chamber consisting of the same context as the first procedure (same geometric shape of chamber, lights, scents, and auditory sounds) for 3 min with no presentation of an unconditioned stimulus or conditioned stimulus. One hour later, the cue test is performed. The cue test chamber consisted of a different geometric shape, flooring, light brightness, and scent compared to the previous chamber used for training. After 3 min in the chamber, the auditory stimulus was presented for 3 min. The software FreezeFrame3 and FreezeView (San Diego Instruments) was used to record and analyze the percent freezing in each trial.

Electrophysiology

Field recordings of Schaffer collateral LTP was performed as described before (*72*). Briefly, brains were isolated from 6.5- to 7-month-old mice and cut into 400 mM slices on a vibratome. Hippocampal slices were incubated for 1 hour at room temperature and then transferred to a heated recording chamber filled with recording artificial cerebrospinal fluid (ACSF) (125 mM NaCl, 2.5 mM KCl, 1.25 mM NaH_2PO_4, 25 mM $NaHCO_3$, 1 mM $MgCl_2$, 2 mM $CaCl_2$, and 10 mM glucose, saturated with 95% O_2 and 5% CO_2) maintained at 32°C. Stimulation of Schaffer collaterals from the CA3 region was performed with bipolar electrodes, whereas borosilicate glass capillary pipettes filled with recording ACSF (resistances of 2 to 3.5 megohms) were used to record field excitatory postsynaptic potentials (fEPSPs) in the CA1 region. Signals were amplified using a MultiClamp 700B amplifier (Axon), digitized using a Digidata 1440A (Axon) with a 2-kHz low-pass filter and a 3-Hz high-pass filter, and then captured and stored using Clampex 10.4 software (Axon) for offline data analysis. The genotypes and treatment groups were blinded to the experimenter. For each experiment, 10 to 13 sections from five to six animals per group per genotype were used.

TPPU measurements and lipidomics

5xFAD mice were treated with TPPU (3 mg/kg) in drinking water for 4 months and then euthanized. Plasma and whole-brain homogenates were extracted and subjected to LC-MS/MS analysis of TPPU and oxylipin on a 4000 QTRAP LC-MS/MS instrument (Applied Biosystems Instrument Corporation). For drug analysis in plasma, 10 μl of plasma samples was transferred to 1.5-μl Eppendorf tubes containing 90 μl of EDTA solution (0.1% EDTA and 0.1% acetic acid), spiked with 10 μl of TPPU-d3 (1 μg/ml) in methanol, and subsequently subjected to liquid-liquid extraction by ethyl acetate (200 μl) twice (*67*). TPPU-d3 was added in each sample as an internal standard solution. The collected extraction solutions were dried using a speed vacuum concentrator, reconstituted in 50 μl of 100 nM 12-[[(cyclohexylamino)carbonyl]amino]-dodecanoic acid (CUDA) in methanol, and ready for LC-MS/MS analysis. TPPU and oxylipin in brain tissues were analyzed simultaneously by a modified LC-MS/MS method (*73*) to including multiple reaction monitoring transition of TPPU. Tissues (~50 mg) were homogenized in ice-cold methanol with 0.1% butylated hydroxytoluene and 0.1% acetic acid. The homogenates were spiked with 10 μl of internal standard solution (mixture of deuterated compounds) and stored at −80°C for 20 hours. After that, the homogenates were extracted using solid-phase extraction (Oasis-HLB Cartridge, Waters). The extracted samples were then collected, dried, and reconstituted in 50 μl of 200 nM CUDA in methanol. The analytes were then detected by the modified LC-MS/MS method.

P-glycoprotein substrate evaluation

Caco-2 cells were diluted to 6.86×10^5 cells/ml with culture medium, and 50 μl of cell suspension was dispensed into the filter well of the 96-well HTS Transwell plate. Cells were cultivated for 14 to 18 days in a cell culture incubator at 37°C, 5% CO_2, and 95% relative humidity. Electrical resistance was measured across the monolayer by using Millicell Epithelial Volt-Ohm measuring system. Transepithelial electrical resistance (TEER) of each well is calculated by the equation: TEER value (ohm·cm^2) = TEER measurement (ohm) × area of membrane (cm^2). The TEER value of each well should be greater than 230 ohm·cm^2. Digoxin was used as the reference substrate of P-gp. Propranolol was used as the high permeability marker. To determine the rate of drug transport in the apical to basolateral direction, working solutions containing TPPU were added to the Transwell insert (apical compartment). To determine the rate of drug transport in the basolateral to apical direction, working solutions

containing TPPU were added to each well of the receiver plate. To determine the rate of drug transport in the presence of a P-gp inhibitor, verapamil, the known inhibitor of P-gp, was added to both apical and basolateral compartments at a final concentration of 100 μM, followed by incubation at 37°C for 2 hours. Next, samples from apical and basolateral wells were transferred to a new 96-well plate, and cold acetonitrile containing appropriate internal standards were added into each well of the plate(s). Samples were analyzed by an LC-MS/MS. Percent parent compounds remaining at each time point are estimated by determining the peak area ratios from extracted ion chromatograms. The apparent permeability coefficient (P_{app}), in units of centimeter per second, was determined using the following equation: P_{app} = (VA × [drug]acceptor) / (area × time × [drug]initial, donor), where VA is the volume (in milliliters) in the acceptor well, area is the surface area of the membrane (0.143 cm^2 for Transwell 96-Well Permeable Supports), and time is the total transport time in seconds. The efflux ratio was determined using the following equation: Efflux ratio = P_{app}(B-A) / P_{app}(A-B), where P_{app}(B-A) indicates the apparent permeability coefficient in basolateral (B) to apical (A) direction and P_{app}(A-B) indicates the apparent permeability coefficient in apical to basolateral direction. The recovery can be determined using the following equation: Recovery % = (VA × [drug]acceptor + VD × [drug]donor) / (VD × [drug]initial, donor), where VA is the volume (in milliliters) in the acceptor well (0.235 ml for Ap → Bl flux and 0.075 ml for Bl → Ap) and VD is the volume (in milliliters) in the donor well (0.075 ml for Ap → Bl flux and 0.235 ml for Bl → Ap).

Quantification and statistical analysis

All data were analyzed with GraphPad Prism version 7.04 and presented as means ± SEM (*$P < 0.05$, **$P < 0.01$, ***$P < 0.001$, and ****$P < 0.0001$). For simple comparisons, Student's t test was used. For multiple comparisons, analysis of variance (ANOVA) followed by the appropriate post hoc testing was used and is specified for each experiment in the figure legends. The statistical tests used for human gene expression analysis are specified in the human gene expression analysis methods section. All samples or animals were included in the statistical analysis unless otherwise specified.

SUPPLEMENTARY MATERIALS

stm.sciencemag.org/cgi/content/full/12/573/eabb1206/DC1

Fig. S1. Altered expression of arachidonic acid pathway genes in the brains of patients with AD and APP^{NLGF} mice.
Fig. S2. LPS induces sEH expression in mouse primary astrocytes in vivo.
Fig. S3. TPPU attenuates LPS-induced up-regulation of sEH and proinflammatory markers in mouse primary astrocytes.
Fig. S4. EET attenuates LPS-induced proinflammatory gene expression in mouse primary microglia.
Fig. S5. EET attenuates LPS-induced inflammation in organotypic mouse hippocampal slice cultures.
Fig. S6. TPPU mitigates LPS-induced proinflammatory gene expression in C57BL/6 mice.
Fig. S7. TPPU mitigates LPS-induced glial cell reactivity in C57BL/6 mice.
Fig. S8. EC5026 reduces LPS-induced inflammation in C57BL/6 mice.
Fig. S9. *Ephx2* gene expression in the brains of 5xFAD transgenic mice of different ages.
Fig. S10. Bioavailability of TPPU in the brains of 5xFAD transgenic mice.
Fig. S11. TPPU reduces glial and immune protein expression in the cortex of 5xFAD transgenic mice.
Fig. S12. Glial cell characteristics in relation to Aβ pathology in the brains of 5xFAD transgenic mice at 4.5 months of age.
Fig. S13. Glial cell characteristics in relation to Aβ pathology in the brains of 5xFAD transgenic mice at 6.5 months of age.
Fig. S14. TPPU does not alter the expression of genes encoding APP processing or Aβ degradation enzymes in the brains of 5xFAD transgenic mice.
Fig. S15. TPPU ameliorates synaptic deficits in the brains of 5xFAD transgenic mice.
Table S1. P-glycoprotein substrate evaluation of TPPU in the Caco-2 cell line.
Table S2. Demographic data for patients with AD and controls providing postmortem brain tissue.
Table S3. Primer sequences for qPCR.
Data file S1. Individual-level data for all figures.

View/request a protocol for this paper from *Bio-protocol*.

REFERENCES AND NOTES

1. H. W. Querfurth, F. M. LaFerla, Alzheimer's disease. *N. Engl. J. Med.* **362**, 329–344 (2010).
2. J. M. Long, D. M. Holtzman, Alzheimer disease: An update on pathobiology and treatment strategies. *Cell* **179**, 312–339 (2019).
3. L. Mucke, D. J. Selkoe, Neurotoxicity of amyloid beta-protein: Synaptic and network dysfunction. *Cold Spring Harb. Perspect. Med.* **2**, a006338 (2012).
4. J. L. Cummings, S. Cohen, C. H. van Dyck, M. Brody, C. Curtis, W. Cho, M. Ward, M. Friesenhahn, C. Rabe, F. Brunstein, A. Quartino, L. A. Honigberg, R. N. Fuji, D. Clayton, D. Mortensen, C. Ho, R. Paul, ABBY: A phase 2 randomized trial of crenezumab in mild to moderate Alzheimer disease. *Neurology* **90**, e1889–e1897 (2018).
5. J. L. Cummings, T. Morstorf, K. Zhong, Alzheimer's disease drug-development pipeline: Few candidates, frequent failures. *Alzheimers Res. Ther.* **6**, 37 (2014).
6. D. R. Elmaleh, M. R. Farlow, P. S. Conti, R. G. Tompkins, L. Kundakovic, R. E. Tanzi, Developing effective Alzheimer's disease therapies: Clinical experience and future directions. *J. Alzheimers Dis.* **71**, 715–732 (2019).
7. M. V. Guillot-Sestier, K. R. Doty, T. Town, Innate immunity fights Alzheimer's disease. *Trends Neurosci.* **38**, 674–681 (2015).
8. M. T. Heneka, M. P. Kummer, A. Stutz, A. Delekate, S. Schwartz, A. Vieira-Saecker, A. Griep, D. Axt, A. Remus, T. C. Tzeng, E. Gelpi, A. Halle, M. Korte, E. Latz, D. T. Golenbock, NLRP3 is activated in Alzheimer's disease and contributes to pathology in APP/PS1 mice. *Nature* **493**, 674–678 (2013).
9. M. T. Heneka, M. P. Kummer, E. Latz, Innate immune activation in neurodegenerative disease. *Nat. Rev. Immunol.* **14**, 463–477 (2014).
10. S. Prokop, K. R. Miller, F. L. Heppner, Microglia actions in Alzheimer's disease. *Acta Neuropathol.* **126**, 461–477 (2013).
11. H. Lian, H. Zheng, Signaling pathways regulating neuron-glia interaction and their implications in Alzheimer's disease. *J. Neurochem.* **136**, 475–491 (2016).
12. B. W. Kunkle, B. Grenier-Boley, R. Sims, J. C. Bis, V. Damotte, A. C. Naj, A. Boland, M. Vronskaya, S. J. van der Lee, A. Amlie-Wolf, C. Bellenguez, A. Frizatti, V. Chouraki, E. R. Martin, K. Sleegers, N. Badarinarayan, J. Jakobsdottir, K. L. Hamilton-Nelson, S. Moreno-Grau, R. Olaso, R. Raybould, Y. Chen, A. B. Kuzma, M. Hiltunen, T. Morgan, S. Ahmad, B. N. Vardarajan, J. Epelbaum, P. Hoffmann, M. Boada, G. W. Beecham, J. G. Garnier, D. Harold, A. L. Fitzpatrick, O. Valladares, M. L. Moutet, A. Gerrish, A. V. Smith, L. Qu, D. Bacq, N. Denning, X. Jian, Y. Zhao, M. Del Zompo, N. C. Fox, S. H. Choi, I. Mateo, J. T. Hughes, H. H. Adams, J. Malamon, F. Sanchez-Garcia, Y. Patel, J. A. Brody, B. A. Dombroski, M. C. D. Naranjo, M. Daniilidou, G. Eiriksdottir, S. Mukherjee, D. Wallon, J. Uphill, T. Aspelund, L. B. Cantwell, F. Garzia, D. Galimberti, E. Hofer, M. Butkiewicz, B. Fin, E. Scarpini, C. Sarnowski, W. S. Bush, S. Meslage, J. Kornhuber, C. C. White, Y. Song, R. C. Barber, S. Engelborghs, S. Sordon, D. Voijnovic, P. M. Adams, R. Vandenberghe, M. Mayhaus, L. A. Cupples, M. S. Albert, P. P. De Deyn, W. Gu, J. J. Himali, D. Beekly, A. Squassina, A. M. Hartmann, A. Orellana, D. Blacker, E. Rodriguez-Rodriguez, S. Lovestone, M. E. Garcia, R. S. Doody, C. Munoz-Fernadez, R. Sussams, H. Lin, T. J. Fairchild, Y. A. Benito, C. Holmes, H. Karamujic-Comic, M. P. Frosch, H. Thonberg, W. Maier, G. Roshchupkin, B. Ghetti, V. Giedraitis, A. Kawalia, S. Li, R. M. Huebinger, L. Kilander, S. Moebus, I. Hernandez, M. I. Kamboh, R. Brundin, J. Turton, Q. Yang, M. J. Katz, L. Concari, J. Lord, A. S. Beiser, C. D. Keene, S. Helisalmi, I. Kloszewska, W. A. Kukull, A. M. Koivisto, A. Lynch, L. Tarraga, E. B. Larson, A. Haapasalo, B. Lawlor, T. H. Mosley, R. B. Lipton, V. Solfrizzi, M. Gill, W. T. Longstreth Jr., T. J. Montine, V. Frisardi, M. Diez-Fairen, F. Rivadeneira, R. C. Petersen, V. Deramecourt, I. Alvarez, F. Salani, A. Ciaramella, E. Boerwinkle, E. M. Reiman, N. Fievet, J. I. Rotter, J. S. Reisch, O. Hanon, C. Cupidi, A. G. A. Uitterlinden, D. R. Royall, C. Dufouil, R. G. Maletta, I. de Rojas, M. Sano, A. Brice, R. Cecchetti, P. S. George-Hyslop, K. Ritchie, M. Tsolaki, D. W. Tsuang, B. Dubois, D. Craig, C. K. Wu, H. Soininen, D. Avramidou, R. L. Albin, L. Fratiglioni, A. Germanou, L. G. Apostolova, L. Keller, M. Koutroumani, S. E. Arnold, F. Panza, O. Gkatzima, S. Asthana, D. Hannequin, P. Whitehead, C. S. Atwood, P. Caffarra, H. Hampel, I. Quintela, A. Carracedo, L. Lannfelt, D. C. Rubinsztein, L. L. Barnes, F. Pasquier, L. Frolich, S. Barral, B. McGuinness, T. G. Beach, J. A. Johnston, J. T. Becker, P. Passmore, E. H. Bigio, J. M. Schott, T. D. Bird, J. D. Warren, B. F. Boeve, M. K. Lupton, J. D. Bowen, P. Proitsi, A. Boxer, J. F. Powell, J. R. Burke, J. S. K. Kauwe, J. M. Burns, M. Mancuso, J. D. Buxbaum, U. Bonuccelli, N. J. Cairns, A. McQuillin, C. Cao, G. Livingston, C. S. Carlson, N. J. Bass, C. M. Carlsson, J. Hardy, R. M. Carney, J. Bras, M. M. Carrasquillo, R. Guerreiro, M. Allen, H. C. Chui, E. Fisher, C. Masullo, E. A. Crocco, C. DeCarli, G. Bisceglio, M. Dick, L. Ma, R. Duara, N. R. Graff-Radford, D. A. Evans, A. Hodges, K. M. Faber, M. Scherer, K. B. Fallon,

M. Riemenschneider, D. W. Fardo, R. Heun, M. R. Farlow, H. Kolsch, S. Ferris, M. Leber, T. M. Foroud, I. Heuser, D. R. Galasko, I. Giegling, M. Gearing, M. Hull, D. H. Geschwind, J. R. Gilbert, J. Morris, R. C. Green, K. Mayo, J. H. Growdon, T. Feulner, R. L. Hamilton, L. E. Harrell, D. Drichel, L. S. Honig, T. D. Cushion, M. J. Huentelman, P. Hollingworth, C. M. Hulette, B. T. Hyman, R. Marshall, G. P. Jarvik, A. Meggy, E. Abner, G. E. Menzies, L. W. Jin, G. Leonenko, L. M. Real, G. R. Jun, C. T. Baldwin, D. Grozeva, A. Karydas, G. Russo, J. A. Kaye, R. Kim, F. Jessen, N. W. Kowall, B. Vellas, J. H. Kramer, E. Vardy, F. M. LaFerla, K. H. Jockel, J. J. Lah, M. Dichgans, J. B. Leverenz, D. Mann, A. I. Levey, S. Pickering-Brown, A. P. Lieberman, N. Klopp, K. L. Lunetta, H. E. Wichmann, C. G. Lyketsos, K. Morgan, D. C. Marson, K. Brown, F. Martiniuk, C. Medway, D. C. Mash, M. M. Nothen, E. Masliah, N. M. Hooper, W. C. McCormick, A. Daniele, S. M. McCurry, A. Bayer, A. N. McDavid, J. Gallacher, A. C. McKee, H. van den Bussche, M. Mesulam, C. Brayne, B. L. Miller, S. Riedel-Heller, C. A. Miller, J. W. Miller, A. Al-Chalabi, J. C. Morris, C. E. Shaw, A. J. Myers, J. Wiltfang, S. O'Bryant, J. M. Olichney, V. Alvarez, J. E. Parisi, A. B. Singleton, H. L. Paulson, J. Collinge, W. R. Perry, S. Mead, E. Peskind, D. H. Cribbs, M. Rossor, A. Pierce, N. S. Ryan, W. W. Poon, B. Nacmias, H. Potter, S. Sorbi, J. F. Quinn, E. Sacchinelli, A. Raj, G. Spalletta, M. Raskind, C. Caltagirone, P. Bossu, M. D. Orfei, B. Reisberg, R. Clarke, C. Reitz, A. D. Smith, J. M. Ringman, D. Warden, E. D. Roberson, G. Wilcock, E. Rogaeva, A. C. Bruni, H. J. Rosen, M. Gallo, R. N. Rosenberg, Y. Ben-Shlomo, M. A. Sager, P. Mecocci, A. J. Saykin, P. Pastor, M. L. Cuccaro, J. M. Vance, J. A. Schneider, L. S. Schneider, S. Slifer, W. W. Seeley, A. G. Smith, J. A. Sonnen, S. Spina, R. A. Stern, R. H. Swerdlow, M. Tang, R. E. Tanzi, J. Q. Trojanowski, J. C. Troncoso, V. M. Van Deerlin, L. J. Van Eldik, H. V. Vinters, J. P. Vonsattel, S. Weintraub, K. A. Welsh-Bohmer, K. C. Wilhelmsen, J. Williamson, T. S. Wingo, R. L. Woltjer, C. B. Wright, C. E. Yu, L. Yu, Y. Saba, A. Pilotto, M. J. Bullido, O. Peters, P. K. Crane, D. Bennett, P. Bosco, E. Coto, V. Boccardi, P. L. De Jager, A. Lleo, N. Warner, O. L. Lopez, M. Ingelsson, P. Deloukas, C. Cruchaga, C. Graff, R. Gwilliam, M. Fornage, A. M. Goate, P. Sanchez-Juan, P. G. Kehoe, N. Amin, N. Ertekin-Taner, C. Berr, S. Debette, S. Love, L. J. Launer, S. G. Younkin, J. F. Dartigues, C. Corcoran, M. A. Ikram, D. W. Dickson, G. Nicolas, D. Campion, J. Tschanz, H. Schmidt, H. Hakonarson, J. Clarimon, R. Munger, R. Schmidt, L. A. Farrer, C. Van Broeckhoven, M. C. O'Donovan, A. L. DeStefano, L. Jones, J. L. Haines, J. F. Deleuze, M. J. Owen, V. Gudnason, R. Mayeux, V. Escott-Price, B. M. Psaty, A. Ramirez, L. S. Wang, A. Ruiz, C. M. van Duijn, P. A. Holmans, S. Seshadri, J. Williams, P. Amouyel, G. D. Schellenberg, J. C. Lambert, M. A. Pericak-Vance, Genetic meta-analysis of diagnosed Alzheimer's disease identifies new risk loci and implicates Aβ, tau, immunity and lipid processing. *Nat. Genet.* **51**, 414–430 (2019).
13. C. Liu, J. Chyr, W. Zhao, Y. Xu, Z. Ji, H. Tan, C. Soto, X. Zhou, Genome-wide association and mechanistic studies indicate that immune response contributes to Alzheimer's disease development. *Front. Genet.* **9**, 410 (2018).
14. R. Guerreiro, J. Bras, J. Hardy, SnapShot: Genetics of Alzheimer's disease. *Cell* **155**, 968–968.e1 (2013).
15. D. Felsky, T. Roostaei, K. Nho, S. L. Risacher, E. M. Bradshaw, V. Petyuk, J. A. Schneider, A. Saykin, D. A. Bennett, P. L. De Jager, Neuropathological correlates and genetic architecture of microglial activation in elderly human brain. *Nat. Commun.* **10**, 409 (2019).
16. C. H. Trepanier, N. W. Milgram, Neuroinflammation in Alzheimer's disease: Are NSAIDs and selective COX-2 inhibitors the next line of therapy? *J. Alzheimers Dis.* **21**, 1089–1099 (2010).
17. I. Cacciatore, L. Marinelli, E. Fornasari, L. S. Cerasa, P. Eusepi, H. Turkez, C. Pomilio, M. Reale, C. D'Angelo, E. Costantini, A. Di Stefano, Novel NSAID-derived drugs for the potential treatment of Alzheimer's disease. *Int. J. Mol. Sci.* **17**, (2016).
18. H. C. Shen, B. D. Hammock, Discovery of inhibitors of soluble epoxide hydrolase: A target with multiple potential therapeutic indications. *J. Med. Chem.* **55**, 1789–1808 (2012).
19. J. W. Phillis, L. A. Horrocks, A. A. Farooqui, Cyclooxygenases, lipoxygenases, and epoxygenases in CNS: Their role and involvement in neurological disorders. *Brain Res. Rev.* **52**, 201–243 (2006).
20. K. Node, Y. Huo, X. Ruan, B. Yang, M. Spiecker, K. Ley, D. C. Zeldin, J. K. Liao, Anti-inflammatory properties of cytochrome P450 epoxygenase-derived eicosanoids. *Science* **285**, 1276–1279 (1999).
21. J. Bystrom, J. A. Wray, M. C. Sugden, M. J. Holness, K. E. Swales, T. D. Warner, M. L. Edin, D. C. Zeldin, D. W. Gilroy, D. Bishop-Bailey, Endogenous epoxygenases are modulators of monocyte/macrophage activity. *PLOS ONE* **6**, e26591 (2011).
22. K. R. Schmelzer, L. Kubala, J. W. Newman, I. H. Kim, J. P. Eiserich, B. D. Hammock, Soluble epoxide hydrolase is a therapeutic target for acute inflammation. *Proc. Natl. Acad. Sci. U.S.A.* **102**, 9772–9777 (2005).
23. X. Fang, Soluble epoxide hydrolase: A novel target for the treatment of hypertension. *Recent Pat. Cardiovasc. Drug Discov.* **1**, 67–72 (2006).
24. V. Y. Ng, Y. Huang, L. M. Reddy, J. R. Falck, E. T. Lin, D. L. Kroetz, Cytochrome P450 eicosanoids are activators of peroxisome proliferator-activated receptor alpha. *Drug Metab. Dispos.* **35**, 1126–1134 (2007).
25. T. R. Harris, B. D. Hammock, Soluble epoxide hydrolase: Gene structure, expression and deletion. *Gene* **526**, 61–74 (2013).
26. Q. Ren, M. Ma, T. Ishima, C. Morisseau, J. Yang, K. M. Wagner, J. C. Zhang, C. Yang, W. Yao, C. Dong, M. Han, B. D. Hammock, K. Hashimoto, Gene deficiency and pharmacological inhibition of soluble epoxide hydrolase confers resilience to repeated social defeat stress. *Proc. Natl. Acad. Sci. U.S.A.* **113**, E1944–E1952 (2016).
27. M. Ma, Q. Ren, J. Yang, K. Zhang, Z. Xiong, T. Ishima, Y. Pu, S. H. Hwang, M. Toyoshima, Y. Iwayama, Y. Hisano, T. Yoshikawa, B. D. Hammock, K. Hashimoto, Key role of soluble epoxide hydrolase in the neurodevelopmental disorders of offspring after maternal immune activation. *Proc. Natl. Acad. Sci. U.S.A.* **116**, 7083–7088 (2019).
28. Q. Ren, M. Ma, J. Yang, R. Nonaka, A. Yamaguchi, K. I. Ishikawa, K. Kobayashi, S. Murayama, S. H. Hwang, S. Saiki, W. Akamatsu, N. Hattori, B. D. Hammock, K. Hashimoto, Soluble epoxide hydrolase plays a key role in the pathogenesis of Parkinson's disease. *Proc. Natl. Acad. Sci. U.S.A.* **115**, e5815–e5823 (2018).
29. H. T. Lee, K. I. Lee, C. H. Chen, T. S. Lee, Genetic deletion of soluble epoxide hydrolase delays the progression of Alzheimer's disease. *J. Neuroinflammation* **16**, 267 (2019).
30. C. Griñán-Ferré, S. Codony, E. Pujol, J. Yang, R. Leiva, C. Escolano, D. Puigoriol-Illamola, J. Companys-Alemany, R. Corpas, C. Sanfeliu, B. Pérez, M. I. Loza, J. Brea, C. Morisseau, B. D. Hammock, S. Vázquez, M. Pallàs, C. Galdeano, Pharmacological inhibition of soluble epoxide hydrolase as a new therapy for Alzheimer's disease. *Neurotherapeutics* 10.1007/s13311-020-00854-1, (2020).
31. T. E. Rose, C. Morisseau, J. Y. Liu, B. Inceoglu, P. D. Jones, J. R. Sanborn, B. D. Hammock, 1-Aryl-3-(1-acylpiperidin-4-yl)urea inhibitors of human and murine soluble epoxide hydrolase: Structure-activity relationships, pharmacokinetics, and reduction of inflammatory pain. *J. Med. Chem.* **53**, 7067–7075 (2010).
32. S. I. Rapoport, Arachidonic acid and the brain. *J. Nutr.* **138**, 2515–2520 (2008).
33. T. Saito, Y. Matsuba, N. Mihira, J. Takano, P. Nilsson, S. Itohara, N. Iwata, T. C. Saido, Single App knock-in mouse models of Alzheimer's disease. *Nat. Neurosci.* **17**, 661–663 (2014).
34. D. B. Swartzlander, N. E. Propson, E. R. Roy, T. Saito, T. Saido, B. Wang, H. Zheng, Concurrent cell type-specific isolation and profiling of mouse brains in inflammation and Alzheimer's disease. *JCI Insight* **3**, (2018).
35. W. Yang, V. R. Tuniki, S. Anjaiah, J. R. Falck, C. J. Hillard, W. B. Campbell, Characterization of epoxyeicosatrienoic acid binding site in U937 membranes using a novel radiolabeled agonist, 20-125i-14,15-epoxyeicosa-8(Z)-enoic acid. *J. Pharmacol. Exp. Ther.* **324**, 1019–1027 (2008).
36. K. M. Gauthier, C. Deeter, U. M. Krishna, Y. K. Reddy, M. Bondlela, J. R. Falck, W. B. Campbell, 14,15-Epoxyeicosa-5(Z)-enoic acid. *Circ. Res.* **90**, 1028–1036 (2002).
37. K. M. Gauthier, S. G. Jagadeesh, J. R. Falck, W. B. Campbell, 14,15-epoxyeicosa-5(Z)-enoic-mSI: A 14,15- and 5,6-EET antagonist in bovine coronary arteries. *Hypertension* **42**, 555–561 (2003).
38. T. H. Hung, S. K. Shyue, C. H. Wu, C. C. Chen, C. C. Lin, C. F. Chang, S. F. Chen, Deletion or inhibition of soluble epoxide hydrolase protects against brain damage and reduces microglia-mediated neuroinflammation in traumatic brain injury. *Oncotarget* **8**, 103236–103260 (2017).
39. M. F. Rosenberg, G. Velarde, R. C. Ford, C. Martin, G. Berridge, I. D. Kerr, R. Callaghan, A. Schmidlin, C. Wooding, K. J. Linton, C. F. Higgins, Repacking of the transmembrane domains of P-glycoprotein during the transport ATPase cycle. *EMBO J.* **20**, 5615–5625 (2001).
40. P. V. Balimane, Y. H. Han, S. Chong, Current industrial practices of assessing permeability and P-glycoprotein interaction. *AAPS J.* **8**, E1–E13 (2006).
41. R. Elsby, D. D. Surry, V. N. Smith, A. J. Gray, Validation and application of Caco-2 assays for the in vitro evaluation of development candidate drugs as substrates or inhibitors of P-glycoprotein to support regulatory submissions. *Xenobiotica* **38**, 1140–1164 (2008).
42. L. Williams, L. Bradley, A. Smith, B. Foxwell, Signal transducer and activator of transcription 3 is the dominant mediator of the anti-inflammatory effects of IL-10 in human macrophages. *J. Immunol.* **172**, 567–576 (2004).
43. S. Krasemann, C. Madore, R. Cialic, C. Baufeld, N. Calcagno, R. El Fatimy, L. Beckers, E. O'Loughlin, Y. Xu, Z. Fanek, D. J. Greco, S. T. Smith, G. Tweet, Z. Humulock, T. Zrzavy, P. Conde-Sanroman, M. Gacias, Z. Weng, H. Chen, E. Tjon, F. Mazaheri, K. Hartmann, A. Madi, J. D. Ulrich, M. Glatzel, A. Worthmann, J. Heeren, B. Budnik, C. Lemere, T. Ikezu, F. L. Heppner, V. Litvak, D. M. Holtzman, H. Lassmann, H. L. Weiner, J. Ochando, C. Haass, O. Butovsky, The TREM2-APOE pathway drives the transcriptional phenotype of dysfunctional microglia in neurodegenerative diseases. *Immunity* **47**, 566–581.e9 (2017).
44. H. Oakley, S. L. Cole, S. Logan, E. Maus, P. Shao, J. Craft, A. Guillozet-Bongaarts, M. Ohno, J. Disterhoft, L. Van Eldik, R. Berry, R. Vassar, Intraneuronal beta-amyloid aggregates, neurodegeneration, and neuron loss in transgenic mice with five familial Alzheimer's disease mutations: Potential factors in amyloid plaque formation. *J. Neurosci.* **26**, 10129–10140 (2006).
45. M. M. Mariani, T. Malm, R. Lamb, T. R. Jay, L. Neilson, B. Casali, L. Medarametla, G. E. Landreth, Neuronally-directed effects of RXR activation in a mouse model of Alzheimer's disease. *Sci. Rep.* **7**, 42270 (2017).
46. S. Kim, Y. Nam, Y. O. Jeong, H. H. Park, S. K. Lee, S. J. Shin, H. Jung, B. H. Kim, S. B. Hong, Y. H. Park, J. Kim, J. Yu, D. H. Yoo, S. H. Park, S. G. Jeon, M. Moon, Topographical visualization of the reciprocal projection between the medial septum and the hippocampus in the 5XFAD mouse model of Alzheimer's disease. *Int. J. Mol. Sci.* **20**, 3992 (2019).

47. W. A. Eimer, R. Vassar, Neuron loss in the 5XFAD mouse model of Alzheimer's disease correlates with intraneuronal Aβ42 accumulation and Caspase-3 activation. *Mol. Neurodegener.* **8**, 2 (2013).
48. B. D. Przybyla-Zawislak, P. K. Srivastava, J. Vazquez-Matias, H. W. Mohrenweiser, J. E. Maxwell, B. D. Hammock, J. A. Bradbury, A. E. Enayetallah, D. C. Zeldin, D. F. Grant, Polymorphisms in human soluble epoxide hydrolase. *Mol. Pharmacol.* **64**, 482–490 (2003).
49. P. K. Srivastava, V. K. Sharma, D. S. Kalonia, D. F. Grant, Polymorphisms in human soluble epoxide hydrolase: Effects on enzyme activity, enzyme stability, and quaternary structure. *Arch. Biochem. Biophys.* **427**, 164–169 (2004).
50. M. Fornage, E. Boerwinkle, P. A. Doris, D. Jacobs, K. Liu, N. D. Wong, Polymorphism of the soluble epoxide hydrolase is associated with coronary artery calcification in African-American Subjects. *Circulation* **109**, 335–339 (2004).
51. K. Ohtoshi, H. Kaneto, K. Node, Y. Nakamura, T. Shiraiwa, M. Matsuhisa, Y. Yamasaki, Association of soluble epoxide hydrolase gene polymorphism with insulin resistance in type 2 diabetic patients. *Biochem. Biophys. Res. Commun.* **331**, 347–350 (2005).
52. J. Hu, S. Dziumbla, J. Lin, S. I. Bibli, S. Zukunft, J. de Mos, K. Awwad, T. Fromel, A. Jungmann, K. Devraj, Z. Cheng, L. Wang, S. Fauser, C. G. Eberhart, A. Sodhi, B. D. Hammock, S. Liebner, O. J. Muller, C. Glaubitz, H. P. Hammes, R. Popp, I. Fleming, Inhibition of soluble epoxide hydrolase prevents diabetic retinopathy. *Nature* **552**, 248–252 (2017).
53. X. H. Qin, Z. Wu, J. H. Dong, Y. N. Zeng, W. C. Xiong, C. Liu, M. Y. Wang, M. Z. Zhu, W. J. Chen, Y. Zhang, Q. Y. Huang, X. H. Zhu, Liver Soluble epoxide hydrolase regulates behavioral and cellular effects of chronic stress. *Cell Rep.* **29**, 3223–3234.e6 (2019).
54. S. A. Liddelow, K. A. Guttenplan, L. E. Clarke, F. C. Bennett, C. J. Bohlen, L. Schirmer, M. L. Bennett, A. E. Munch, W. S. Chung, T. C. Peterson, D. K. Wilton, A. Frouin, B. A. Napier, N. Panicker, M. Kumar, M. S. Buckwalter, D. H. Rowitch, V. L. Dawson, T. M. Dawson, B. Stevens, B. A. Barres, Neurotoxic reactive astrocytes are induced by activated microglia. *Nature* **541**, 481–487 (2017).
55. L. E. Clarke, S. A. Liddelow, Neurobiology: Diversity reaches the stars. *Nature* **548**, 396–397 (2017).
56. Y. Shi, K. Yamada, S. A. Liddelow, S. T. Smith, L. Zhao, W. Luo, R. M. Tsai, S. Spina, L. T. Grinberg, J. C. Rojas, G. Gallardo, K. Wang, J. Roh, G. Robinson, M. B. Finn, H. Jiang, P. M. Sullivan, C. Baufeld, M. W. Wood, C. Sutphen, L. McCue, C. Xiong, J. L. Del-Aguila, J. C. Morris, C. Cruchaga, A. M. Fagan, B. L. Miller, A. L. Boxer, W. W. Seeley, O. Butovsky, B. A. Barres, S. M. Paul, D. M. Holtzman, ApoE4 markedly exacerbates tau-mediated neurodegeneration in a mouse model of tauopathy. *Nature* **549**, 523–527 (2017).
57. D. Tejera, D. Mercan, J. M. Sanchez-Caro, M. Hanan, D. Greenberg, H. Soreq, E. Latz, D. Golenbock, M. T. Heneka, Systemic inflammation impairs microglial Abeta clearance through NLRP3 inflammasome. *EMBO J.* **38**, e101064 (2019).
58. M. H. Park, M. Lee, G. Nam, M. Kim, J. Kang, B. J. Choi, M. S. Jeong, K. H. Park, W. H. Han, E. Tak, M. S. Kim, J. Lee, Y. Lin, Y. H. Lee, I. S. Song, M. K. Choi, J. Y. Lee, H. K. Jin, J. S. Bae, M. H. Lim, N,N′-Diacetyl-p-phenylenediamine restores microglial phagocytosis and improves cognitive defects in Alzheimer's disease transgenic mice. *Proc. Natl. Acad. Sci. U.S.A.* **116**, 23426–23436 (2019).
59. M. W. Salter, B. Stevens, Microglia emerge as central players in brain disease. *Nat. Med.* **23**, 1018–1027 (2017).
60. H. Sarlus, M. T. Heneka, Microglia in Alzheimer's disease. *J. Clin. Invest.* **127**, 3240–3249 (2017).
61. A. Litvinchuk, Y. W. Wan, D. B. Swartzlander, F. Chen, A. Cole, N. E. Propson, Q. Wang, B. Zhang, Z. Liu, H. Zheng, Complement C3aR inactivation attenuates tau pathology and reverses an immune network deregulated in tauopathy models and Alzheimer's disease. *Neuron* **100**, 1337–1353.e5 (2018).
62. Q. Shi, S. Chowdhury, R. Ma, K. X. Le, S. Hong, B. J. Caldarone, B. Stevens, C. A. Lemere, Complement C3 deficiency protects against neurodegeneration in aged plaque-rich APP/PS1 mice. *Sci. Transl. Med.* **9**, eaaf6295 (2017).
63. S. Zarriello, J. P. Tuazon, S. Corey, S. Schimmel, M. Rajani, A. Gorsky, D. Incontri, B. D. Hammock, C. V. Borlongan, Humble beginnings with big goals: Small molecule soluble epoxide hydrolase inhibitors for treating CNS disorders. *Prog. Neurobiol.* **172**, 23–39 (2019).
64. A. Ulu, S. Appt, C. Morisseau, S. H. Hwang, P. D. Jones, T. E. Rose, H. Dong, J. Lango, J. Yang, H. J. Tsai, C. Miyabe, C. Fortenbach, M. R. Adams, B. D. Hammock, Pharmacokinetics and in vivo potency of soluble epoxide hydrolase inhibitors in cynomolgus monkeys. *Br. J. Pharmacol.* **165**, 1401–1412 (2012).
65. Y. Liu, X. Lu, S. Nguyen, J. L. Olson, H. K. Webb, D. L. Kroetz, Epoxyeicosatrienoic acids prevent cisplatin-induced renal apoptosis through a p38 mitogen-activated protein kinase-regulated mitochondrial pathway. *Mol. Pharmacol.* **84**, 925–934 (2013).
66. K. S. Lee, J. Y. Liu, K. M. Wagner, S. Pakhomova, H. Dong, C. Morisseau, S. H. Fu, J. Yang, P. Wang, A. Ulu, C. A. Mate, L. V. Nguyen, S. H. Hwang, M. L. Edin, A. A. Mara, H. Wulff, M. E. Newcomer, D. C. Zeldin, B. D. Hammock, Optimized inhibitors of soluble epoxide hydrolase improve in vitro target residence time and in vivo efficacy. *J. Med. Chem.* **57**, 7016–7030 (2014).
67. D. Wan, J. Yang, C. B. McReynolds, B. Barnych, K. M. Wagner, C. Morisseau, S. H. Hwang, J. Sun, R. Blocher, B. D. Hammock, In vitro and in vivo metabolism of a potent inhibitor of soluble epoxide hydrolase, 1-(1-propionylpiperidin-4-yl)-3-(4-(trifluoromethoxy) phenyl)urea. *Front. Pharmacol.* **10**, 464 (2019).
68. A. Ghosh, T. Tyson, S. George, E. N. Hildebrandt, J. A. Steiner, Z. Madaj, E. Schulz, E. Machiela, W. G. McDonald, M. L. Escobar Galvis, J. H. Kordower, J. M. Van Raamsdonk, J. R. Colca, P. Brundin, Mitochondrial pyruvate carrier regulates autophagy, inflammation, and neurodegeneration in experimental models of Parkinson's disease. *Sci. Transl. Med.* **8**, 368ra174 (2016).
69. A. Ghosh, M. R. Langley, D. S. Harischandra, M. L. Neal, H. Jin, V. Anantharam, J. Joseph, T. Brenza, B. Narasimhan, A. Kanthasamy, B. Kalyanaraman, A. G. Kanthasamy, Mitoapocynin treatment protects against neuroinflammation and dopaminergic neurodegeneration in a preclinical animal model of Parkinson's disease. *J. Neuroimmune Pharmacol.* **11**, 259–278 (2016).
70. A. Ghosh, A. Kanthasamy, J. Joseph, V. Anantharam, P. Srivastava, B. P. Dranka, B. Kalyanaraman, A. G. Kanthasamy, Anti-inflammatory and neuroprotective effects of an orally active apocynin derivative in pre-clinical models of Parkinson's disease. *J. Neuroinflammation* **9**, 241 (2012).
71. W. Guo, A. M. Allan, R. Zong, L. Zhang, E. B. Johnson, E. G. Schaller, A. C. Murthy, S. L. Goggin, A. J. Eisch, B. A. Oostra, D. L. Nelson, P. Jin, X. Zhao, Ablation of Fmrp in adult neural stem cells disrupts hippocampus-dependent learning. *Nat. Med.* **17**, 559–565 (2011).
72. H. Lian, L. Yang, A. Cole, L. Sun, A. C. Chiang, S. W. Fowler, D. J. Shim, J. Rodriguez-Rivera, G. Taglialatela, J. L. Jankowsky, H. C. Lu, H. Zheng, NFκB-activated astroglial release of complement C3 compromises neuronal morphology and function associated with Alzheimer's disease. *Neuron* **85**, 101–115 (2015).
73. J. Yang, K. Schmelzer, K. Georgi, B. D. Hammock, Quantitative profiling method for oxylipin metabolome by liquid chromatography electrospray ionization tandem mass spectrometry. *Anal. Chem.* **81**, 8085–8093 (2009).

Acknowledgments: We are grateful to V. Lee and J. Trojanowski (University of Pennsylvania) for providing postmortem AD patient brain tissues and T. Saito and T. Saido (RIKEN Brain Science Institute) for the APP^{NLGF} knock-in mice. We thank B. Contreras and N. Aithmitti for expert technical assistance, B. Wang and E. Roy for help with organotypic culture and NanoString nCount panel experiments, and members of the Zheng laboratory for insightful discussions. We acknowledge support from the Genomic and RNA Profiling Core and the Cytometry and Cell Sorting Core at Baylor College of Medicine for NanoString and FACS analyses, respectively. **Funding:** This project was supported by grants from the NIH (R01 NS093652, R01 AG020670, RF1 AG054111, R01 AG057509, and RF1 062257 to H.Z.) and NIEHS (RIVER Award R35 ES030443-01 and Superfund Research Program P42 ES04699 to B.D.H.)
Author contributions: A.G. and H.Z. designed the overall study. A.G. performed all in vitro and in vivo assays and associated biochemical and immunohistochemical experiments as well as data analysis, with technical assistance from M.M.C. and N.E.P. M.M.C. and F.C. performed mouse behavioral tests and LTP recordings and associated data analysis, respectively. S.H.H. and B.D.H. provided TPPU and advised on the related experiments. D.W. performed mass spectrometry analysis of oxylipins. A.G. and H.Z. wrote the manuscript, and all authors read, provided input, and approved the manuscript. **Competing interests:** S.H.H. is a part-time employee and B.D.H. is a cofounder and CEO of EicOsis LLC. H.Z. is on the Scientific Advisory Board of the Tau Consortium managed by the Rainwater Charitable Foundation. **Data and materials availability:** All data associated with this study are present in the paper or the Supplementary Materials. Gene expression data have been deposited in NCBI with GEO accession number GSE161848. TPPU and EC5026 are commercially available from Cayman (MI, USA) and MedChemExpress (NJ, USA), respectively.

Submitted 31 January 2020
Accepted 26 August 2020
Published 9 December 2020
10.1126/scitranslmed.abb1206

Citation: A. Ghosh, M. M. Comerota, D. Wan, F. Chen, N. E. Propson, S. H. Hwang, B. D. Hammock, H. Zheng, An epoxide hydrolase inhibitor reduces neuroinflammation in a mouse model of Alzheimer's disease. *Sci. Transl. Med.* **12**, eabb1206 (2020).

Science Translational Medicine

An epoxide hydrolase inhibitor reduces neuroinflammation in a mouse model of Alzheimer's disease

Anamitra Ghosh, Michele M. Comerota, Debin Wan, Fading Chen, Nicholas E. Propson, Sung Hee Hwang, Bruce D. Hammock and Hui Zheng

Sci Transl Med **12**, eabb1206.
DOI: 10.1126/scitranslmed.abb1206

Dialing up epoxy fatty acids in the brain

Neuroinflammation is strongly implicated in Alzheimer's disease (AD). The epoxy lipids produced from arachidonic acid have anti-inflammatory properties, but they are rapidly turned over by the soluble epoxide hydrolase (sEH). Ghosh *et al*. now report that sEH is elevated in the brains of patients with AD and in an amyloid mouse model of AD, suggesting that blocking sEH may replenish the epoxy lipids and combat neuroinflammation. Treating AD mice with a small-molecule inhibitor of sEH restored the epoxy lipids, reduced neuroinflammation and amyloid pathology, and improved cognition. This study identifies a lipid metabolic pathway regulating neuroinflammation and provides support for further development of sEH inhibitors as a potential treatment for AD.

Science Translational Medicine
AAAS

stm.sciencemag.org/cgi/content/full/12/573/eabb1206/DC1

Supplementary Materials for

An epoxide hydrolase inhibitor reduces neuroinflammation in a mouse model of Alzheimer's disease

Anamitra Ghosh, Michele M. Comerota, Debin Wan, Fading Chen, Nicholas E. Propson, Sung Hee Hwang, Bruce D. Hammock, Hui Zheng*

*Corresponding author. Email: huiz@bcm.edu

Published 9 December 2020, *Sci. Transl. Med.* **12**, eabb1206 (2020)
DOI: 10.1126/scitranslmed.abb1206

The PDF file includes:

Table S2. Demographic data for patients with AD and controls providing postmortem brain tissue.

Table S3. Primer sequences for qPCR.

Other Supplementary Material for this manuscript includes the following:

(available at stm.sciencemag.org/cgi/content/full/12/573/eabb1206/DC1)

Data file S1 (Microsoft Excel format). Individual-level data for all figures.

Supplementary Materials

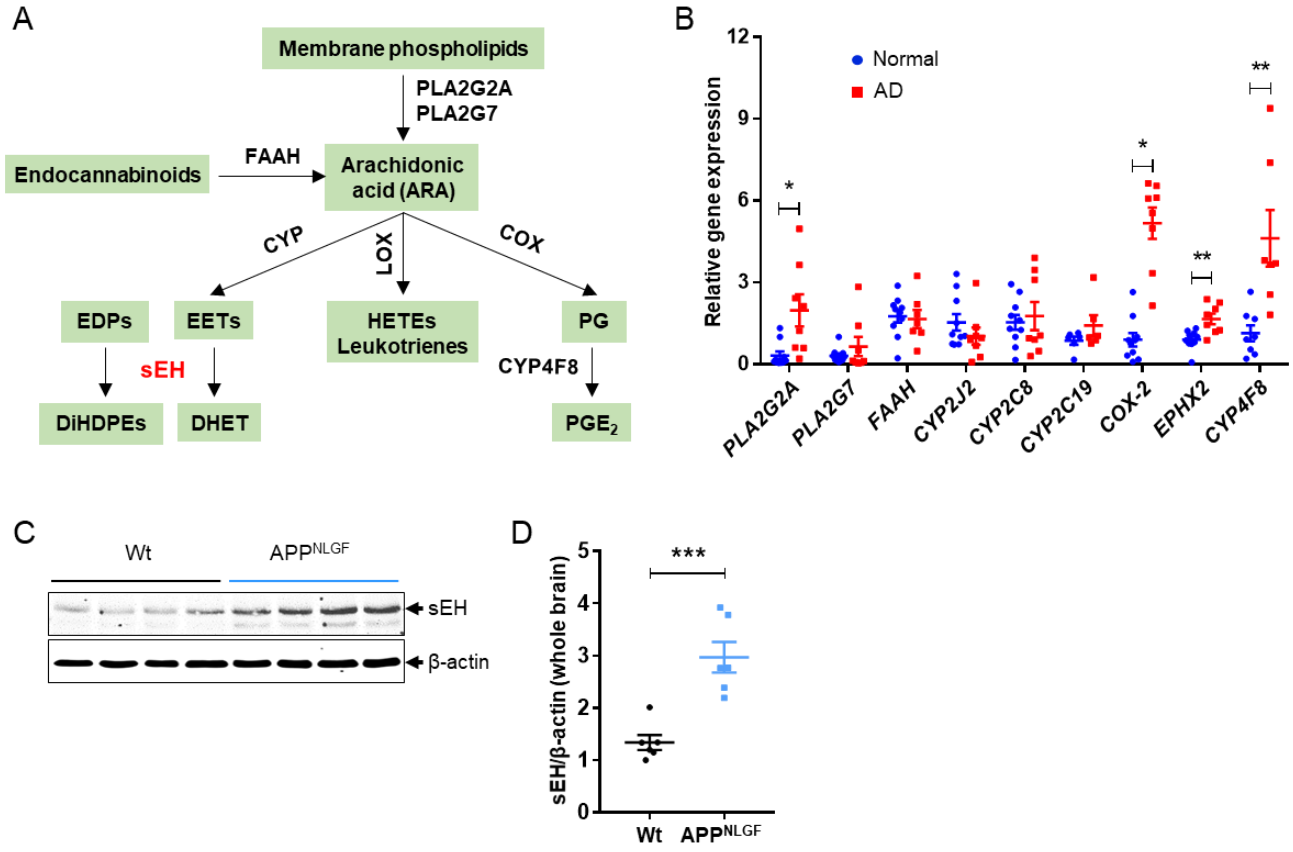

Fig. S1. Altered expression of arachidonic acid pathway genes in the brains of patients with AD and APP^{NLGF} mice. (A) Schematic diagram of arachidonic acid (ARA) metabolism pathway. (B) qPCR analysis of mRNA expression of ARA pathway genes in postmortem brain tissue from AD patients (n=8) and age-matched cognitively normal controls (n=10). (C) Representative Western blot of sEH in bulk brain samples of littermate wild-type (Wt) and homozygous APP^{NLGF} mice at 6.5 months of age. (D) Scattered dot plot showing mean sEH/β-actin ratio. Values are expressed as means ± SEM of six mice per group (mixed gender). ***P < 0.001. Data were analyzed unpaired Student's *t*-test.

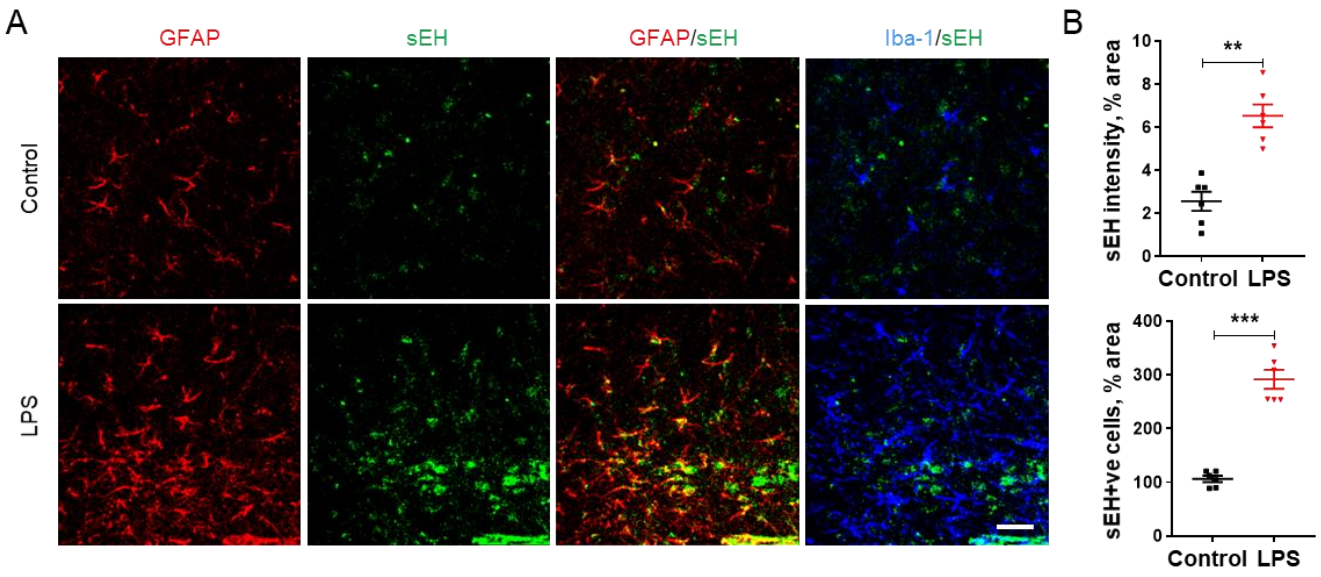

Fig. S2. LPS induces sEH expression in mouse primary astrocytes in vivo. (A) Immunofluorescence staining of GFAP (red), sEH (green), and Iba-1 (blue) of hippocampal sections of C57BL/6 mice treated with vehicle (Control) or LPS for 18 hours. Scale bar: 50 μm. (B) Quantification of sEH intensity (top) and sEH +ve cells (bottom). Values are expressed as means ± SEM of six mice per group of mixed gender. ***P < 0.001, **P < 0.01. Data were analyzed by unpaired Student's *t*-test.

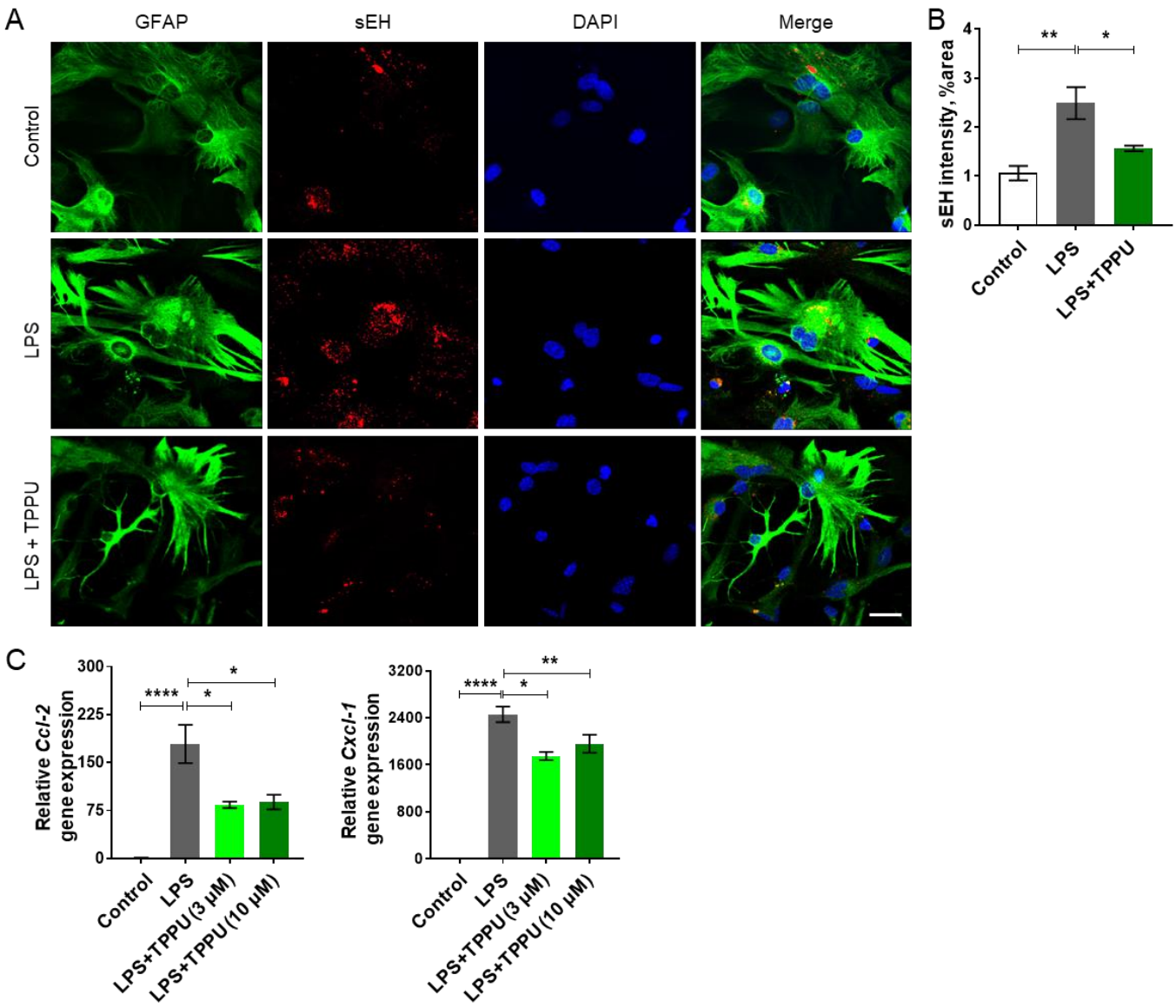

Fig. S3. TPPU attenuates LPS-induced up-regulation of sEH and proinflammatory markers in mouse primary astrocytes. Primary astrocytes were pretreated with TPPU (3 μM and 10 μM) for 30 minutes followed by LPS treatment (100 ng/ml) for 24 h. (A) Double immunofluorescence of GFAP (green) and sEH (red) in non-treated astrocytes (Control) or astrocytes treated with LPS alone or LPS with 10 μM TPPU. DAPI (blue) stains nucleus. Scale bar: 100 μm. (B) Quantification of sEH intensity. (C) qPCR analysis of mRNA expression of *Ccl-2* and *Cxcl-1*. Data are means ± SEM of three

independent experiments. ****P < 0.0001, **P < 0.01, *P < 0.05. Data were analyzed by one-way ANOVA with Tukey's multiple comparison test

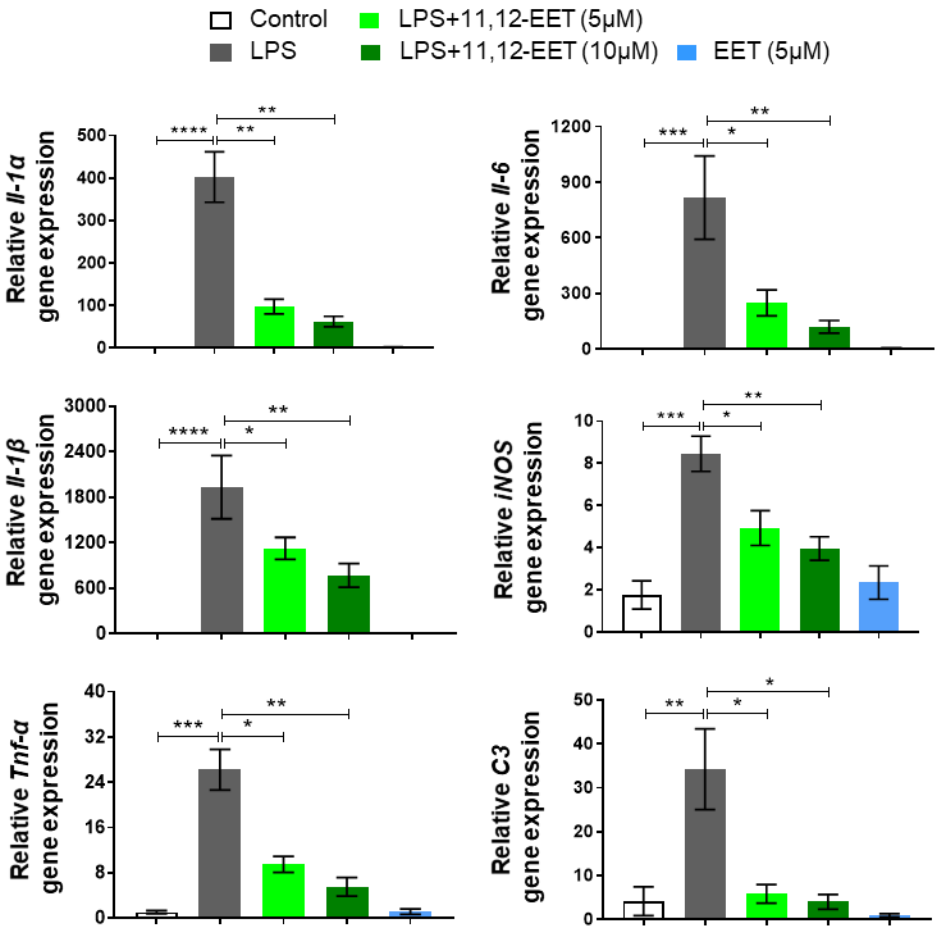

Fig. S4. EET attenuates LPS-induced proinflammatory gene expression in mouse primary microglia. qPCR analysis of mRNA expression of *Il-1α*, *Il-1β*, *Tnf-α*, *Il-6*, *iNOS* and *C3* in primary microglia: non-treated (Control), treated with LPS alone (LPS) or pretreated with 5 μM or 10 μM of 11,12-EET for 30 minutes followed by LPS treatment (100 ng/ml) for 24 h. Data are means ± SEM of three independent experiments. ****P < 0.0001, ***P < 0.001, **P < 0.01, *P < 0.05. Data were analyzed by one-way ANOVA with Tukey's multiple comparison test.

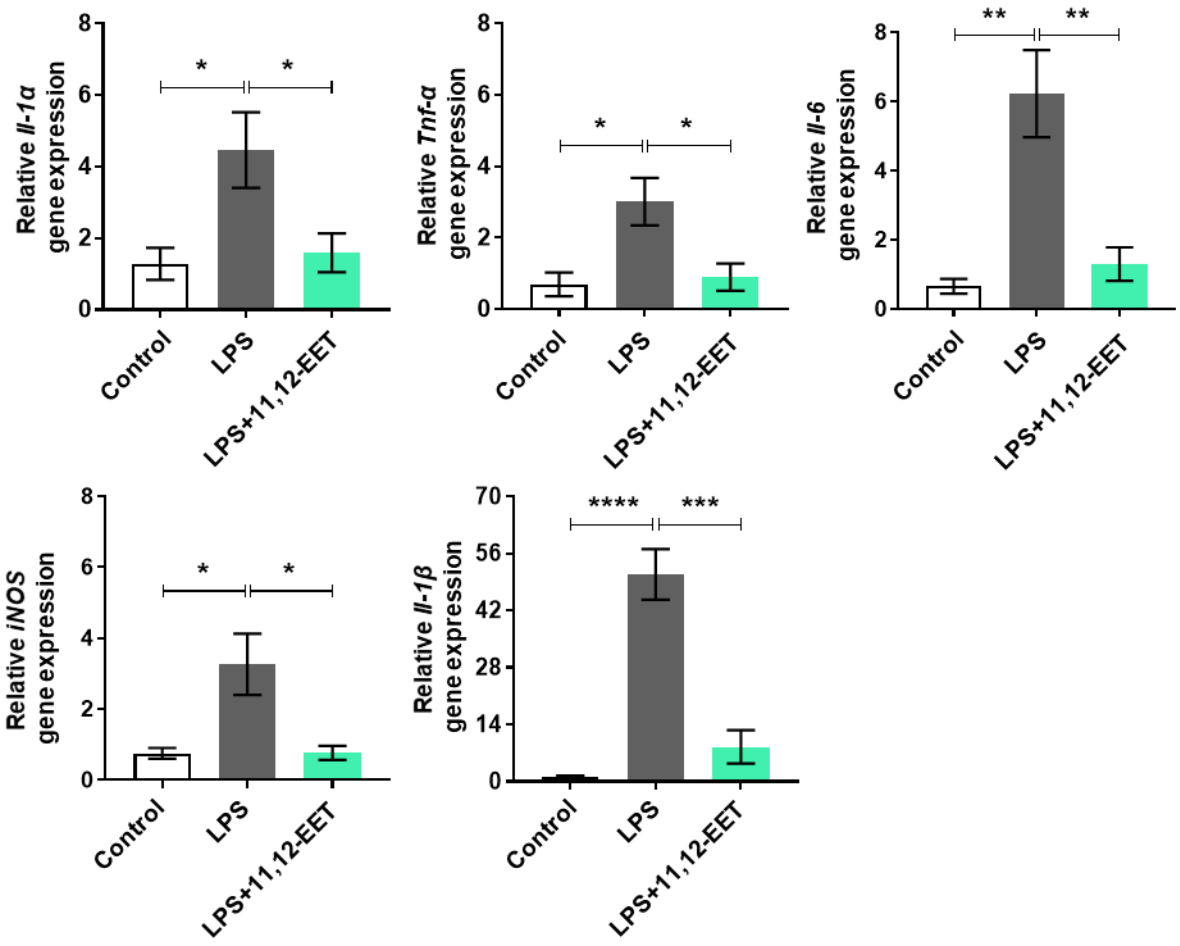

Fig. S5. EET attenuates LPS-induced inflammation in organotypic mouse hippocampal slice cultures. qPCR analysis of mRNA expression of proinflammatory molecules as indicated in hippocampal slices from C57BL/6 mice that are non-treated (Control), treated with LPS alone (LPS), or pretreated with 11,12-EET (5 μM) for 30 minutes followed by LPS treatment (100 ng/ml) for 24 h (LPS+11,12-EET). Data are means ± SEM of three independent experiments. ****P < 0.0001, ***P < 0.001, **P < 0.01, *P < 0.05. Data were analyzed by one-way ANOVA with Tukey's multiple comparison test.

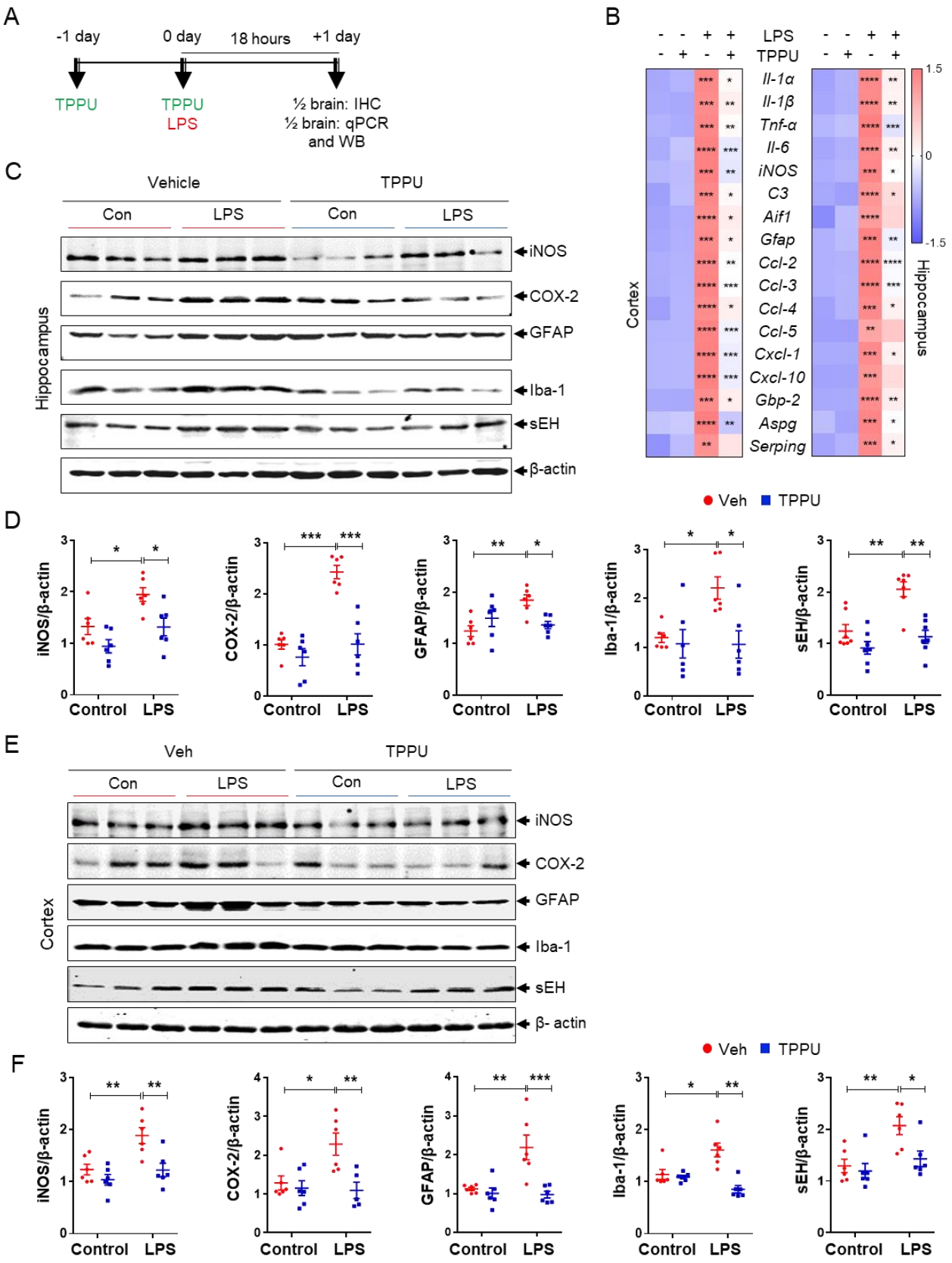
A
-1 day
0 day
18 hours
+1 day
TPPU
TPPU
LPS
½ brain: IHC
½ brain: qPCR
and WB
B
LPS
TPPU
Il-1α
Il-1β
Tnf-α
Il-6
iNOS
C3
Aif1
Gfap
Ccl-2
Ccl-3
Ccl-4
Ccl-5
Cxcl-1
Cxcl-10
Gbp-2
Aspg
Serping
Cortex
Hippocampus
1.5
0
-1.5
C
Vehicle
TPPU
Con
LPS
Con
LPS
Hippocampus
iNOS
COX-2
GFAP
Iba-1
sEH
β-actin
Veh
TPPU
D
iNOS/β-actin
COX-2/β-actin
GFAP/β-actin
Iba-1/β-actin
sEH/β-actin
Control
LPS
E
Veh
TPPU
Con
LPS
Con
LPS
Cortex
iNOS
COX-2
GFAP
Iba-1
sEH
β- actin
F
Veh
TPPU
iNOS/β-actin
COX-2/β-actin
GFAP/β-actin
Iba-1/β-actin
sEH/β-actin
Control
LPS

Fig. S6. TPPU mitigates LPS-induced proinflammatory gene expression in C57BL/6 mice. (A) Schematic diagram showing TPPU treatment. Mice were pretreated with TPPU (3 mg/kg, oral gavage) 1 day before (-1d) LPS administration. On day 0 (0d) mice were co-treated with LPS (3 mg/kg, i.p.) and TPPU (3 mg/kg, oral gavage) for 18 hours. Vehicle-treated mice were used as controls (Control). (B) Heat map visualization of qPCR analysis of mRNA expression in cortex (left) and in hippocampus (right). The asterisks in LPS (+) TPPU (-) column represent significant changes vs LPS (-) TPPU (-). The asterisks in LPS (+) TPPU (+) represent significant change vs LPS (+) TPPU (-). (C) Representative Western blot illustrating the levels of iNOS, COX-2, GFAP, Iba-1 and sEH in hippocampus. (D) Scattered dot plot showing mean Western blot protein expression over β-actin in hippocampus. (E) Representative Western blot illustrating the expression iNOS, COX-2, GFAP, Iba-1 and sEH in cortex. (F) Scattered dot plot showing mean Western blot protein expression over β-actin in cortex. Data are means ± SEM of six to eight mice per group of mixed gender. ***$P < 0.001$, **$P < 0.01$, *$P < 0.05$. Data were analyzed by one-way ANOVA with Tukey's multiple comparison test.

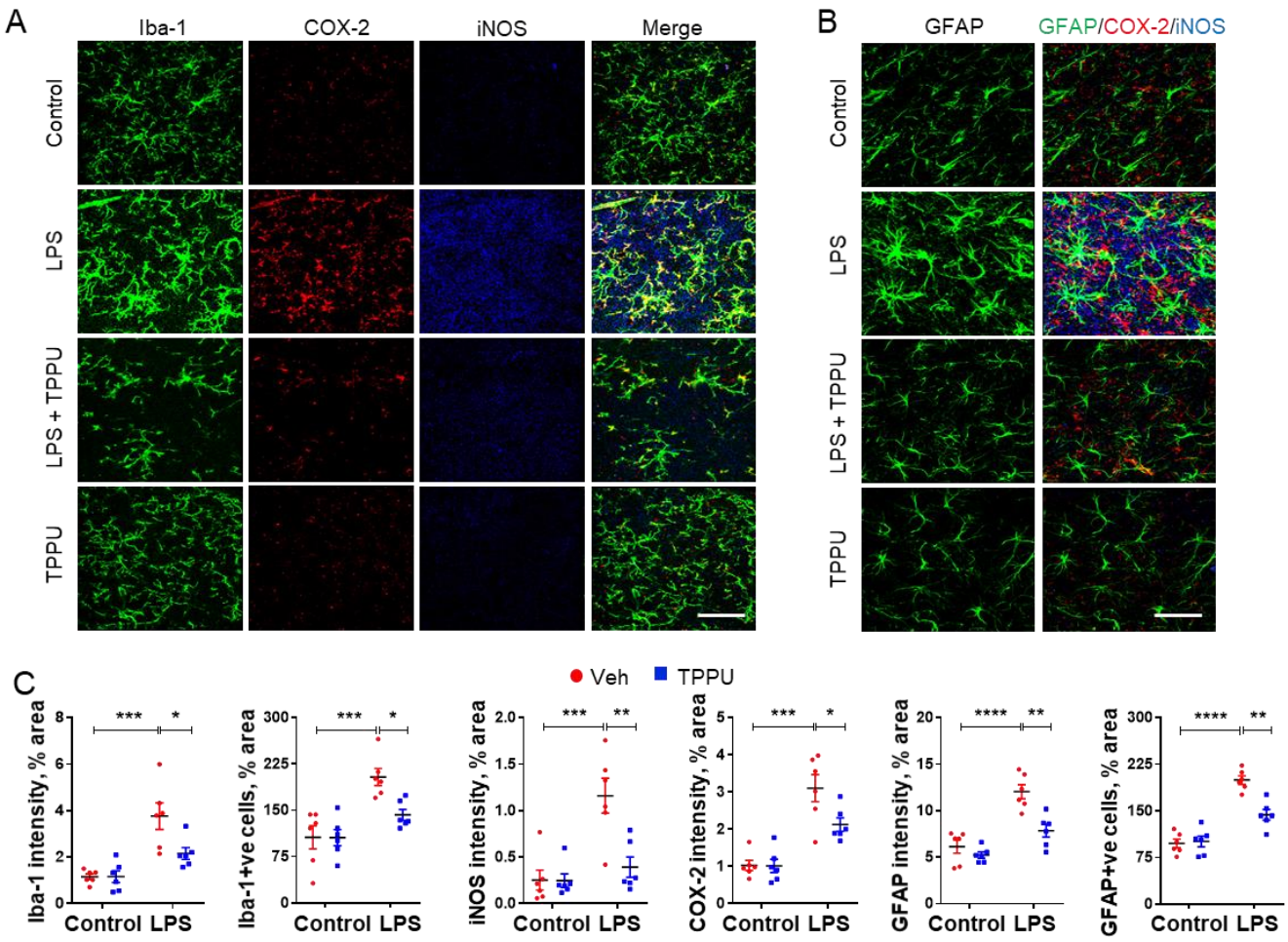

Fig. S7. TPPU mitigates LPS-induced glial cell reactivity in C57BL/6 mice. (A) Triple immunofluorescence staining of Iba-1 (green), COX-2 (red) and iNOS (blue) in hippocampus of mice treated with LPS, TPPU or LPS + TPPU as outlined in fig. S6a. Scale bar, 100 μm. (B) Immunofluorescence staining of GFAP (left) and merged panel of GFAP (green), COX-2 (red) and iNOS (blue) (right). Scale bar, 75 μm. (C) Quantification of Iba-1, iNOS, COX-2 and GFAP intensities and Iba-1+ve and GFAP+ve cells in the hippocampus. Data are means ± SEM of six to eight mice per group (mixed gender). ****P < 0.0001, ***P < 0.001, **P < 0.01, *P < 0.05. Data were analyzed by one-way ANOVA with Tukey's multiple comparison test.

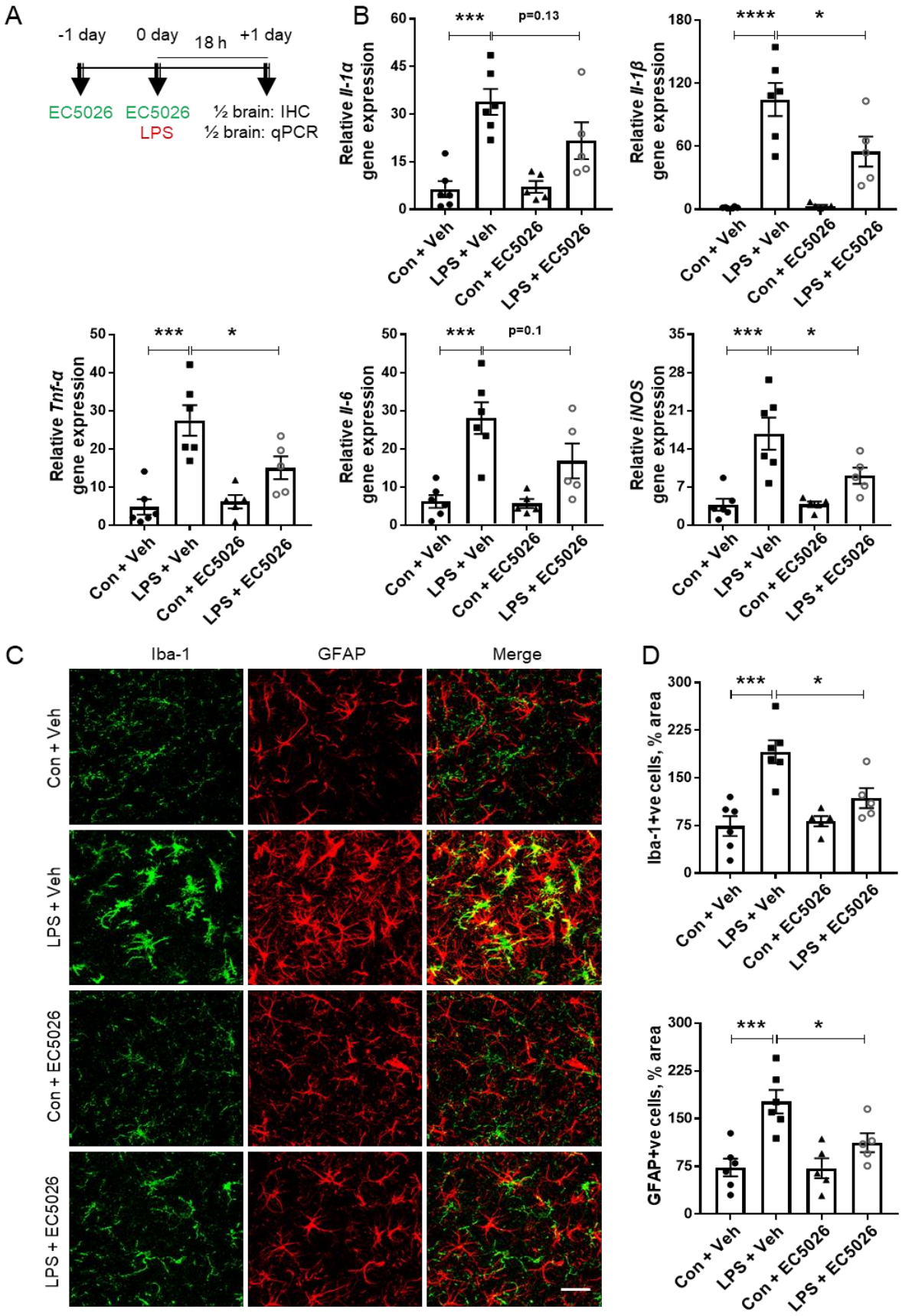
A
-1 day
0 day
18 h
+1 day
EC5026
EC5026
LPS
½ brain: IHC
½ brain: qPCR
B
Relative Il-1α gene expression
***
p=0.13
Relative Il-1β gene expression
****
*
Relative Tnf-α gene expression
***
*
Relative Il-6 gene expression
***
p=0.1
Relative iNOS gene expression
***
*
Con + Veh
LPS + Veh
Con + EC5026
LPS + EC5026
C
Iba-1
GFAP
Merge
Con + Veh
LPS + Veh
Con + EC5026
LPS + EC5026
D
Iba-1+ve cells, % area
GFAP+ve cells, % area
***
*

Fig. S8. EC5026 reduces LPS-induced inflammation in C57BL/6 mice. (A) Schematic diagram showing TPPU treatment. Mice were pretreated with EC5026 (3 mg/kg, oral gavage) 1 day before (-1d) LPS administration. On day 0 (0d) mice were co-treated with LPS (3 mg/kg, i.p.) and EC5026 (3 mg/kg, oral gavage) for 18 hours. Veh: vehicle for EC5026; Con: non-LPS control. (B) qPCR analysis of mRNA expression of *Il-1α, Il-1β, TNF-α, IL-6* and *iNOS* in hippocampus. (C) Immunofluorescence staining of Iba-1 (green) and GFAP (red) in hippocampus. Scale bar, 75 μm. (D) Quantification of Iba-1+ve (top) and GFAP+ve (bottom) cells. Data are means ± SEM of five to six mice per group of mixed gender. ****P < 0.0001, ***P < 0.001, *P < 0.05. Data were analyzed by one-way ANOVA with Tukey's multiple comparison test.

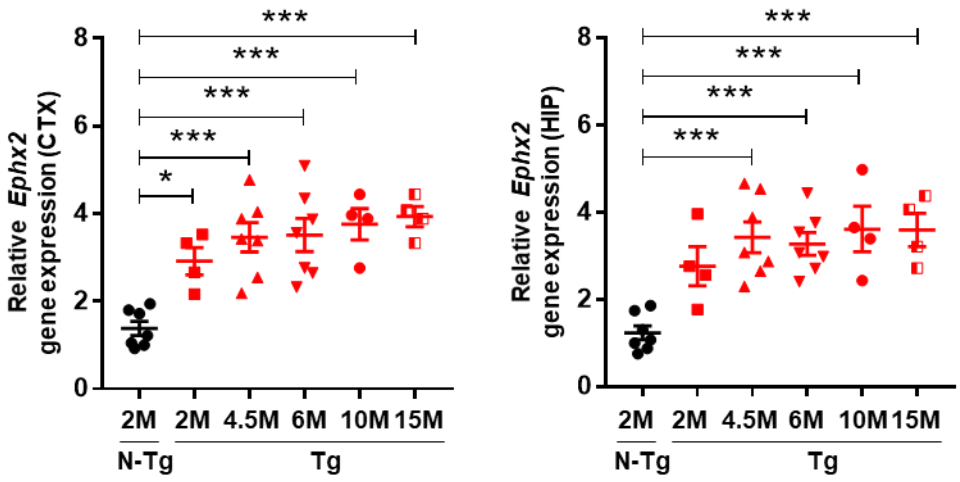

Fig. S9. *Ephx2* gene expression in the brains of 5xFAD transgenic mice of different ages. qPCR analysis of *Ephx2* in cortex (CTX) and in hippocampus (HIP) of non-transgenic (N-Tg) and 5xFAD transgenic (Tg) mice at different ages. 'M' in the X-axis denotes months. Data are means ± SEM of four to seven mice per group of mixed gender. ***P < 0.001, *P < 0.05. Data were analyzed by one-way ANOVA with Tukey's multiple comparison test.

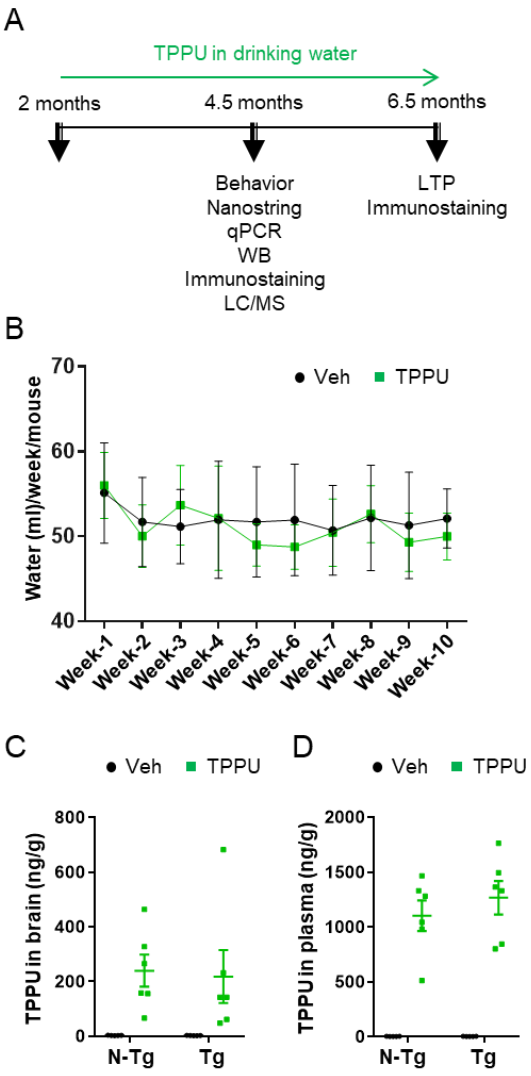

Fig. S10. Bioavailability of TPPU in the brains of 5xFAD transgenic mice. (A) Schematic diagram showing TPPU treatment and analysis. TPPU treatment starts at 2 months of age and continues for either 2.5 months (terminal age 4.5 months) or 4.5 months (terminal age 6.5 months). At 4.5 months mice underwent behavioral experiments. Brains were processed for analyses as indicated. At 6.5 months mice were euthanized for LTP and immunostaining of synaptic and neuronal proteins. (B) Weekly average drinking water consumption per Tg mouse giving either vehicle (Veh) or TPPU. (C) The brain homogenates or (D) plasma were extracted and analyzed by LC/MS for concentrations of TPPU. Data

are means ± SEM of six to eight mice per group of mixed gender. Data were analyzed by two-way ANOVA with Bonferroni's multiple comparison test.

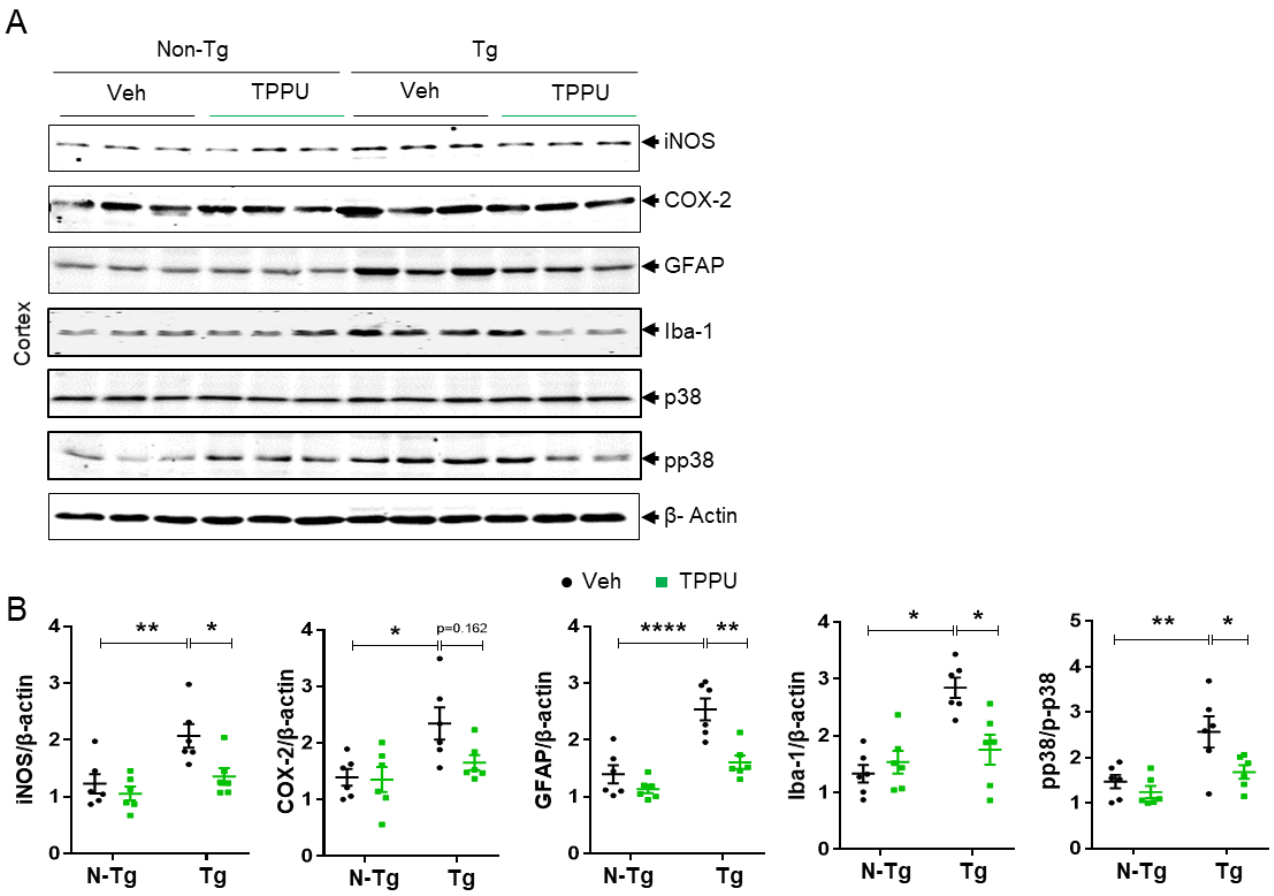

Fig. S11. TPPU reduces glial and immune protein expression in the cortex of 5xFAD transgenic mice. (A) Representative Western blot of iNOS, COX-2, GFAP, Iba-1, p38 and pp38 in the cortex of N-Tg and Tg mice treated with vehicle (Veh) or TPPU starting at 2 months for 2.5 months. β-actin was used as a control. (B) Scattered dot plot showing mean protein expression over β-actin. Data are means ± SEM of six to eight mice per group of mixed gender. ****P < 0.0001, **P < 0.01, *P < 0.05. Data were analyzed by two-way ANOVA with Bonferroni's multiple comparison test.

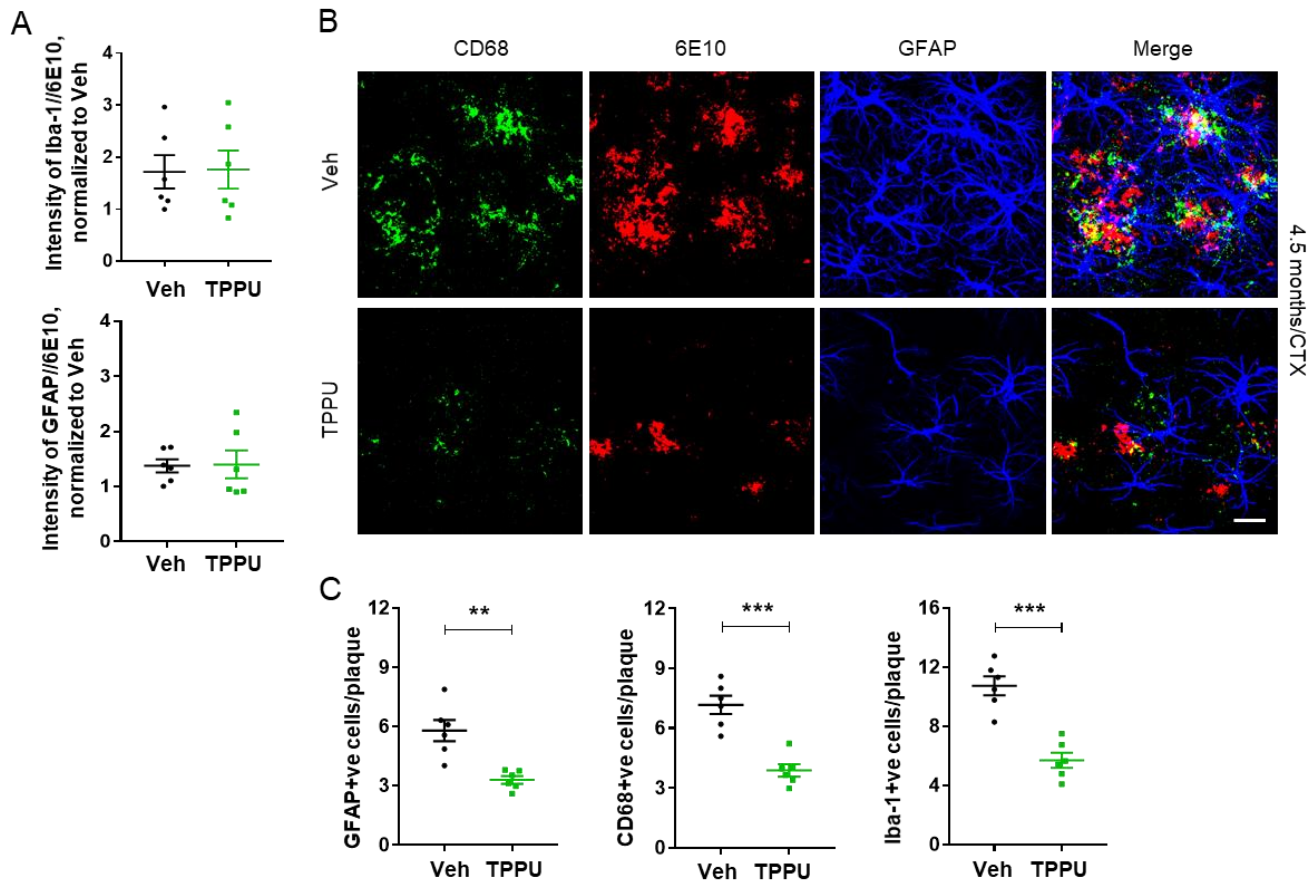

Fig. S12. Glial cell characteristics in relation to Aβ pathology in the brains of 5xFAD transgenic mice at 4.5 months of age. (A) Ratio of intensity of Iba-1 to 6E10 (top) and GFAP to 6E10 (bottom) in the hippocampus of Tg mice treated with vehicle (Veh) or TPPU. Iba-1 and GFAP intensity were measured within 100 μm radius of the plaque. (B) Representative images of CD68 (green), 6E10 (red) and GFAP (blue) in the cortex of 4.5 months Veh or TPPU treated Tg mice. Scale bar: 100 μm. (C) Quantification of GFAP+ve cells, CD68+ve cells and Iba-1+ve cells within 100 μm radius of a plaque (86 to 123 plaques per group were counted). Data are means ± SEM of six to eight mice per group of mixed genders. ***P < 0.001, **P < 0.01. Data were analyzed by Student's *t*-test.

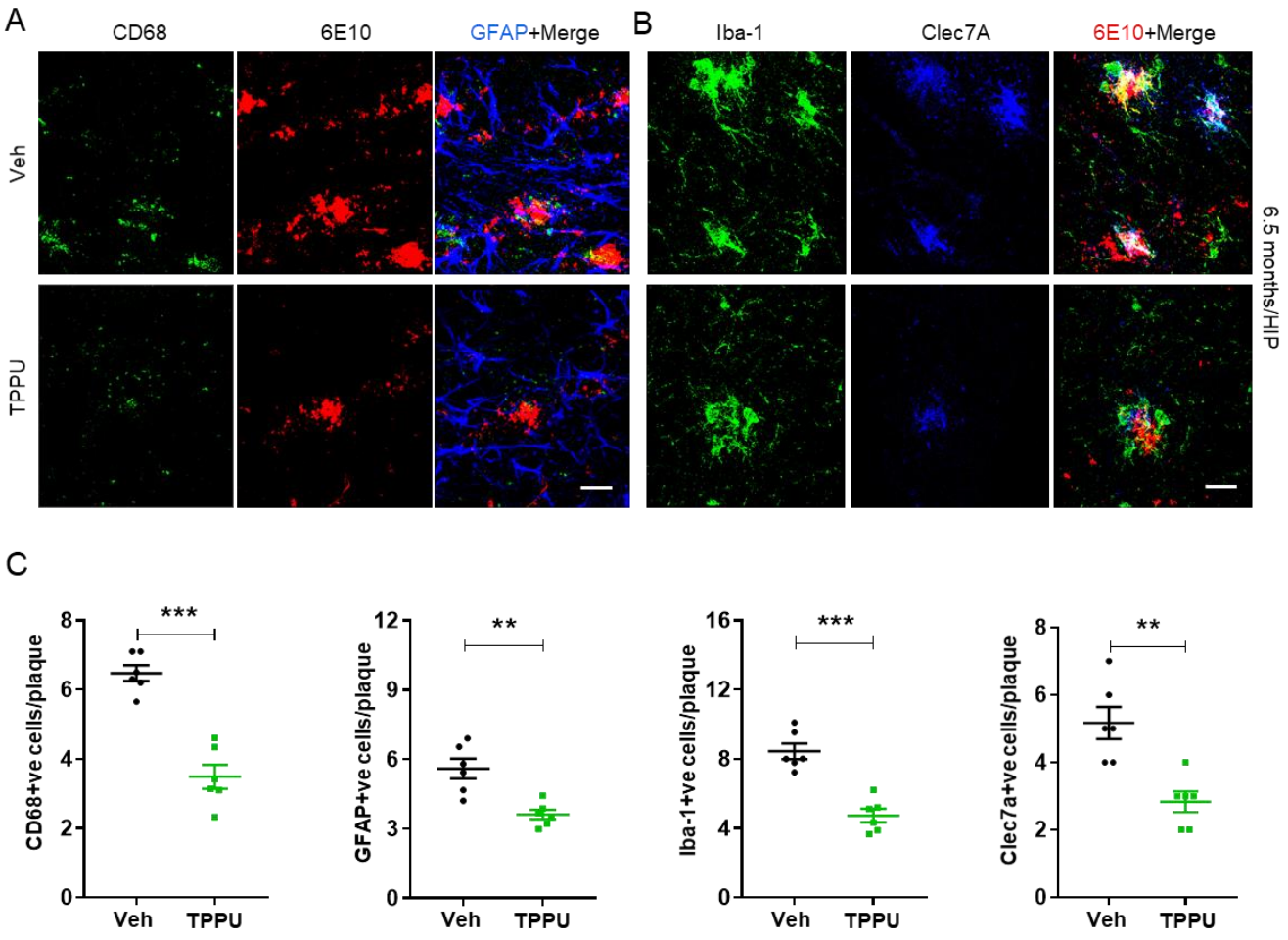

Fig. S13. Glial cell characteristics in relation to Aβ pathology in the brains of 5xFAD transgenic mice at 6.5 months of age. Representative images of (A) CD68 (green), 6E10 (red) and GFAP (blue) and (B) Iba-1 (green), Clec7a (blue) and 6E10 (red) in the hippocampus from 6.5 months old Veh or TPPU treated Tg mice. Scale bar 100 μm. (C) Quantification of CD68+ve cells, GFAP+ve cells, Iba-1+ve cells and Clec7a+ve cells within 100 μm radius of a plaque (86 to 123 plaques per group were counted). Data are means ± SEM of six to eight mice per group of mixed gender. ***P < 0.001, **P < 0.01. Data were analyzed by Student's *t*-test.

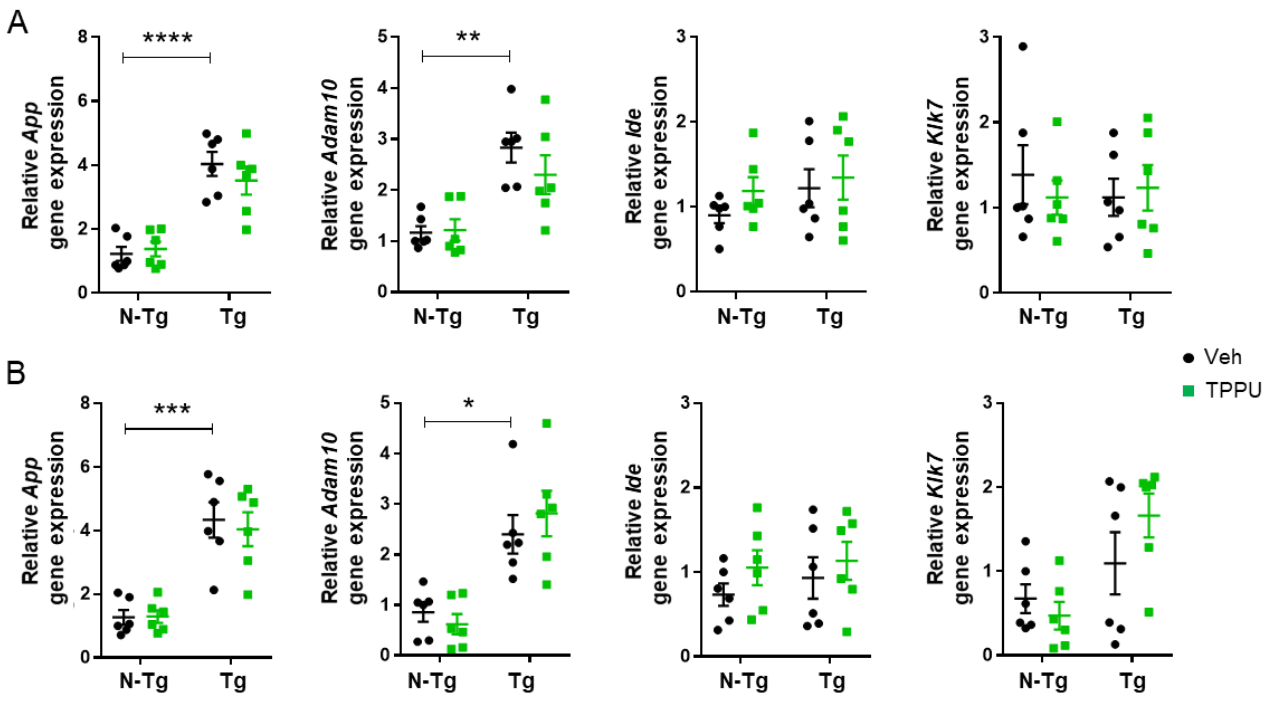

Fig. S14. TPPU does not alter the expression of genes encoding APP processing or Aβ degradation enzymes in the brains of 5xFAD transgenic mice. qPCR analysis of mRNA expression of *App*, *Adam10*, *Ide* and *Klk7* in cortex (A) and hippocampus (B) of N-Tg or Tg mice treated with vehicle (Veh) or TPPU starting at 2 months for 2.5 months. Data are means ± SEM of six to eight mice per group of mixed gender. ****P < 0.0001, ***P < 0.001, **P < 0.01, *P < 0.05. Non-significant between Veh and TPPU within each genotype. Data were analyzed by two-way ANOVA with Bonferroni's multiple comparison test.

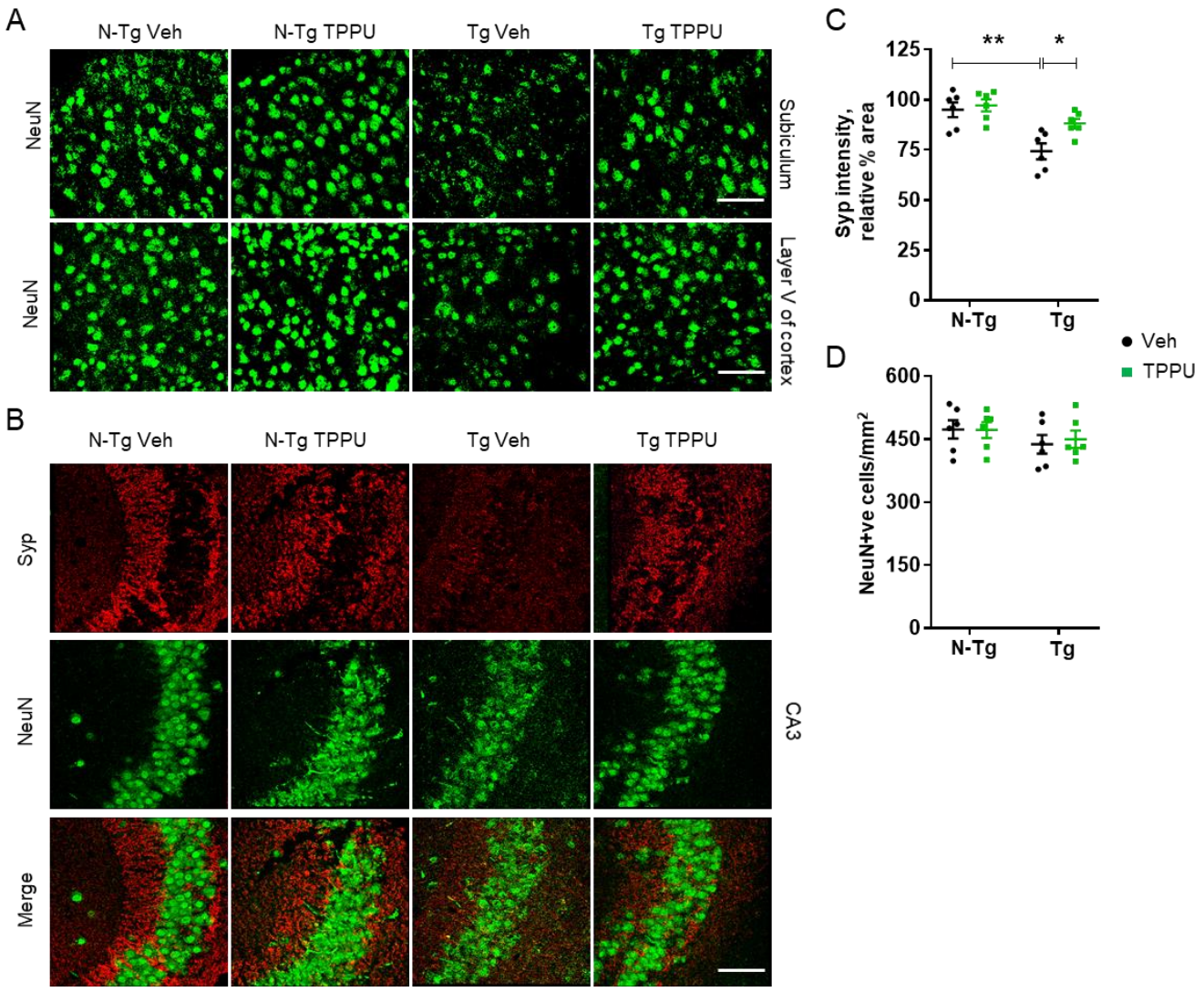

Fig. S15. TPPU ameliorates synaptic deficits in the brains of 5xFAD transgenic mice. (A) Representative NeuN immunostaning images in subiculum and layer V of cortex of N-Tg and Tg mice treated with vehicle (Veh) or TPPU starting at 2 months for 4.5 months. (B) Representative images of synaptophysin (Syp) and NeuN co-immunostaining of area CA3 of hippocampus of N-Tg and Tg mice treated with vehicle (Veh) or TPPU starting at 2 months for 2.5 months. Scale bars, 200 μm. (C) Quantification of Syp intensity. (D) Quantification of NeuN+ve cells. Values are expressed as mean ± SEM of six mice per group of mixed gender. **P < 0.01, *P < 0.05. Data were analyzed by two-way ANOVA with Bonferroni's multiple comparison test.

Table S1. P-glycoprotein substrate evaluation of TPPU in the Caco-2 cell line.

Compound ID	Concentration (μM)	verapamil (μM)	$P_{app\ (A-B)}$ (10^{-6}, cm/s)	$P_{app\ (B-A)}$ (10^{-6}, cm/s)	Efflux Ratio	Recovery (%) AP-BL	Recovery (%) BL-AP
Propranolol	5	-	25.31	15.94	0.63	74.93	85.28
	5	100	30.78	19.84	0.64	89.34	94.12
Digoxin	5	-	0.35	19.70	56.24	94.90	94.54
	5	100	4.52	6.06	1.34	109.30	98.99
TPPU	5	-	18.03	24.45	1.36	80.88	85.49
	5	100	19.50	19.29	0.99	80.75	84.75

Table S2. Demographic data for patients with AD and controls providing postmortem brain tissue.

INDDID	Diagnosis	Sex	Age
109650	AD	Female	64
115165	AD	Male	64
120851	AD	Male	64
106029	AD	Male	71
121576	AD	Male	69
101034	AD	Male	67
116620	AD	Female	55
112723	AD	Male	72
117504	Normal	Male	59
113695	Normal	Female	59
102215	Normal	Female	65
100786	Normal	Male	61
101799	Normal	Male	70
103376	Normal	Female	68
107712	Normal	Male	70
110602	Normal	Male	55
113818	Normal	Female	65
116519	Normal	Female	67

Table S3. Primer sequences for qPCR. Prefix ‘h’ denotes human and ‘m’ denotes mouse.

Gene	Forward (5’-3’)	Reverse (3’-5’)
mEphx2	CCACTCTAGGCCACAGCCTT	CCAAGCAGGAAGTCTCTGGAAA
hEphx2	GTGACCGGAATCCAGCTTCTCAATA	CCAAGAATACCAACTCTCGGGAAAT
mCyp2c39	GAGGAAGCATTCCAATGGTAGAA	TGTGAAGCGCCTAATCTCTTTC
mCyp2j5	TCTGGGAAGCACTCCATCTCA	CCCTGGTGGGTAGTTTTTGG
mCyp2j9	TGGCTGATTTCCTCAAAAACCG	ACTGCTGAAGGGATAGGTGGG
hFaah	CTCTGCTGCCAAGGCTGT	TGCAGTTCCCAGAGTTTTCC
hCyp4f81	CATCTTCAGCTTTGACAGCAA	TGAGCTCCATGATCGCAGTA
hPla2g2a	ACCTGCCCTGTCTCCAAAC	TTTGTTCTGCACTCCTGCTC
hPlag7	TGGCTCTACCTTAGAACCCTGA	TTTTGCTCTTTGCCGTACCT
mIL-1α	CGCTTGAGTCGGCAAAGAAAT	CTTCCCGTTGCTTGACGTTG
mIL-1β	GCAACTGTTCCTGAACTCAACT	ATCTTTTGGGGTCCGTCAACT
mIL-6	TAGTCCTTCCTACCCCAATTTCC	TTGGTCCTTAGCCACTCCTTC
mTNF-α	CCCTCACACTCAGATCATCTTCT	GCTACGACGTGGGCTACAG
miNOS	CCCTTCCGAAGTTTCTGGCAGCAGC	GGCTGTCAGAGCCTCGTGGCTTTGG
mC3	AAG CAT CAA CAC ACC CAA CA	CTT GAG CTC CAT TCG TGA CA
mGfap	AGAAAGGTTGAATCGCTGGA	CGGCGATAGTCGTTA
mAif-1	CAGACTGCCAGCCTAAGACA	AGGAATTGCTTGTTGATCCC
mCcl-2	GAAGGAATGGGTCCAGACAT	ACGGGTCAACTTCACATTCA
mCcl-3	CTCCCAGCCAGGTGTCATTTTC	AGGCATTCAGTTCAGGTCAG
mCcl-4	CCAACTTCCTGCTGTTTCTCT	GTCTGCCTCTTTTGGTCAGGA
mCcl-5	GTGCCCACGTCAAGGAGTAT	CCACTTCTTCTCTGGGTTGG
mCxcl-1	ACCCAAACCGAAGTCATAGCC	TTGTCAGAAGCCAGCGTT
mCxcl-10	CCCACGTGTTGAGATCATTG	CACTGGGTAAAGGGGAGTGA
mGbp-2	GGGGTCACTGTCTGACCACT	GGGAAACCTGGGATGAGATT
mAspg	GCTGCTGGCCATTTACACTG	GTGGGCCTGTGCATACTCTT
mSerping	ACAGCCCCCTCTGAATTCTT	GGATGCTCTCCAAGTTGCTC
mAmigo-2	GAGGCGACCATAATGTCGTT	GCATCCAACAGTCCGATTCT
m18s	CCATTCGAACGTCTGCCCTAT	GTCACCCGTGGTCACCATG
hGapdh	AGGGCTGCTTTTAACTCTGGT	CCCCACTTGATTTTGGAGGGA
mCD68	ACTGGTGTAGCCTAGCTGGT	CCTTGGGCTATAAGCGGTCC
mCox-2	TTCAACACACTCTATCACTGGC	AGAAGCGTTTGCGGTACTCAT
mC1q	AAAGGCAATCCAGGCAATATCA	TGGTTCTGGTATGGACTCTCC
hCyp2j2	ACTGTCGCCTTTCTGCTCG	CTGCTCGAAGTCCACAAGGAA
hCyp2c8	AGATCAGAATTTTCTCACCC	AACTTCGTGTAAGAGCAACA
hCyp2c19	TGCTCTCCTTCTCCTGCTGAAG	TGCCAACGACACGTTCAATC
hCox-2	GAATGGGGTGATGAGCAGTT	CAGAAGGGCAGGATACAGC
mClec7a	ATGGTTCTGGGAGGATGGAT	CCTGGGGAGCTGTATTTCTG

mCst7	AGTCCCATGTCAGCAAAGCC	ATATAGAGTCCGCTTCAAGGCA
mTmem119	GTGTCTAACAGGCCCCAGAA	AGCCACGTGGTATCAAGGAG
mP2ry12	AAAATGCCTGCTGCTTGAAT	TGAAGAAATTCCAACAAAACGA
mCx3cr1	CAGCATCGACCGGTACCTT	GCTGCACTGTCCGGTTGTT
mItgax	CTGGATAGCCTTTCTTCTGCTG	GCACACTGTGTCCGAACTCA
mKlk7	TGGGTGCGAGCCTTCTTTAC	GCTGTCTTTAGCCCTGGAAACC
mAdam10	GAGAGGAAAGAAAGTGGCAGA	AGTGGGTGGGTTAATGAGCA
mIDE	CCGGCCATCCAGAGAATAGAA	ACGGTATTCCCGTTTGTCTTCA
hAPP	ACAGAATTCGCCCCGGCCTGGTAC	TAAGCTTGGCACGGCTGTCCAAGGA